Computer solutions of complex biological boundary-value problems
by Reed Allen Parker

A thesis submitted in partial fulfillment of the requirements for the degree of Master of Science in Electrical Engineering
Montana State University

Abstract:
The subject of this thesis is to predict the induced spatial current density distribution in biological systems due to a time varying magnetic field. Maxwell's equations are solved using an iterative technique known as the Relaxation Method. Results indicate that the induced spatial currents are a strong function of the particular boundaries of the system being studied. Variations of more than an order of magnitude in a small area are found for some idealized bone fractures. Also the direction of flow tends to be parallel to the bone rather than across the gap as is commonly assumed.

COMPUTER SOLUTIONS OF COMPLEX BIOLOGICAL BOUNDARY-VALUE PROBLEMS

by

Reed Allen Parker

A thesis submitted in partial fulfillment
of the requirements for the degree

of

Master of Science

in

Electrical Engineering

MONTANA STATE UNIVERSITY
Bozeman, Montana

March 1984

APPROVAL

of a thesis submitted by

Reed Allen Parker

This thesis has been read by each member of the thesis committee and has been found to be satisfactory regarding content, English usage, format, citations, bibliographic style, and consistency, and is ready for submission to the College of Graduate Studies.

5/7/84
Date

Bruce R. McLeod
Chairperson, Graduate Committee

Approved for the Major Department

5/7/84
Date

D. A. Pierre
Head, Major Department

Approved for the College of Graduate Studies

5/10/84
Date

Henry L Parsons
Graduate Dean

STATEMENT OF PERMISSION TO USE

In presenting this thesis in partial fulfillment of the requirements for a master's degree at Montana State University, I agree that the Library shall make it available to borrowers under rules of the Library. Brief quotations from this thesis are allowable without special permission, provided that accurate acknowledgment of source is made.

Permission for extensive quotation from or reproduction of this thesis may be granted by my major professor, or in his absence, by the Director of Libraries when, in the opinion of either, the proposed use of the material is for scholarly purposes. Any copying or use of the material in this thesis for financial gain shall not be allowed without my written permission.

Signature Reed A. Parker

Date 7-May-1984

ACKNOWLEDGMENTS

The author would like to thank LaJolla Technology Inc., LaJolla, CA and the Engineering Experiment Station (EES) at Montana State University for funding this work. He is especially grateful to Dr. Bruce McLeod for the suggestions, support, and encouragement during this project. The author is most thankful, however, for the support given to him from his wife and parents.

TABLE OF CONTENTS

TABLE OF CONTENTS--CONTINUED

LIST OF FIGURES

LIST OF FIGURES--Continued

LIST OF FIGURES--Continued

ABSTRACT

The subject of this thesis is to predict the induced spatial current density distribution in biological systems due to a time varying magnetic field. Maxwell's equations are solved using an iterative technique known as the Relaxation Method. Results indicate that the induced spatial currents are a strong function of the particular boundaries of the system being studied. Variations of more than an order of magnitude in a small area are found for some idealized bone fractures. Also the direction of flow tends to be parallel to the bone rather than across the gap as is commonly assumed.

CHAPTER 1

INTRODUCTION

The effects of low level electromagnetic energy on biological systems have been documented in several carefully designed experiments [1-4]. This effect can range from increasing the lifespan of mice infected with melanomas (in conjunction with chemotherapy)[1], to modulating the rate of bone fracture healing [2], to adversely affecting the growth of damaged embryos [3]. The exact coupling mechanism between the cell and electromagnetic field is still unknown. In order to determine what this coupling mechanism is, experiments must be designed to have a tight control of variables. Temperature, the process used to test the hypothesis, the system being used, and the electromagnetic fields (both spatially and in the time domain) stimulating the system should be monitored.

Until recently the spatial electric currents induced in biological systems by Helmholz coils were for the most part ignored. McLeod and Sampsel [5,6] have demonstrated that the spatial currents that are introduced into some biological systems can vary by an order of magnitude or more in a very small space. Since the exact coupling mechanism isn't known, researchers should be aware of both the spatial current densities and magnetic fields in their systems.

The work done by McLeod and Sampsel was aimed at simple boundaries whose solution could be determined analytically. In many cases boundar-

ies do not lend themselves to a straightforward analytic solution. The main contribution of this thesis is to present a numerical method to solve some of these complex boundary value problems. Two main systems are looked at separately. A rectangular conducting box is used to verify that the method is accurate, and an idealized two-dimensional bone fracture with different types of bone-flesh boundaries at the site of the fracture is examined in more detail.

Another point that will be addressed in this thesis is how to present the data from these models so that variety of research personnel in such diverse fields as biology, medicine, and engineering can use it. Four methods will be used varying from regular graphs to "three dimensional" views of the system. These methods will be applied to a simple example (a square box) to show how they may be used in conjunction with each other. Finally the bone models will be presented.

CHAPTER 2

THE RELAXATION METHOD APPLIED TO ELECTROMAGNETICS FIELD PROBLEMS

Derivation of the Difference Equation

The differential equation for the $\bar{H}$ field can be derived by starting with Maxwell's fourth equation,

$$\nabla \times \bar{H} = \sigma\bar{E} + \partial(\epsilon\bar{E})/\partial t. \tag{1}$$

Assuming the second term on the right hand side of the equation is small compared to the first term (see discussion on pages 6 and 7 under "assumptions") and taking the curl of both sides yields

$$\nabla(\nabla \cdot \bar{H}) - \nabla^2 \bar{H} = \nabla \times \sigma\bar{E}. \tag{2}$$

The first term on the left hand side is equal to 0 by Maxwell's second equation

$$\nabla \cdot \mu\bar{H} = 0. \tag{3}$$

Substituting Maxwell's third equation,

$$\nabla \times \bar{E} = -\partial(\mu\bar{H})/\partial t, \tag{4}$$

into the right hand side of (2) yields

$$\nabla^2 \bar{H} = \mu\sigma\partial\bar{H}/\partial t. \tag{5}$$

It is seen that this is an equation only in $\bar{H}$. After this equation has been solved the current density $\bar{J}$ can be calculated from (1)

$$\sigma\bar{E} = \bar{J} = \nabla \times \bar{H}. \tag{6}$$

For a two-dimensional case (X-Y plane) with only a Z component of the $\bar{H}$ field, (5) and (6) reduce to

$$\partial^2 H_z/\partial x^2 + \partial^2 H_z/\partial y^2 = \mu\sigma\partial H_z/\partial t, \tag{7}$$

$$J_x = \partial H_z/\partial y, \tag{8}$$

$$J_y = -\partial H_z/\partial x. \tag{9}$$

Equation (7) can be approximated with a difference equation. If we take the continuous function $H_z(x,y)$ and approximate it with a discrete set of points Hx_n,y_n, then the spatial derivatives $\partial^2 H_z/\partial x^2$ can be approximated by the difference equation

$$\partial^2 H_z/\partial x^2 \simeq (Hx_{n+1},y_n + Hx_{n-1},y_n - 2Hx_n,y_n)/\Delta x^2, \tag{10}$$

where Δx is the distance between two consecutive points. If we assume the grid spacing is square ($\Delta x = \Delta y$) with a value of $\Delta 1$ and then substitute the difference approximation into (7), we get the equation for the relaxation method [7],

$$Hx_n,y_n = (Hx_{n-1},y_n + Hx_n,y_{n-1} + Hx_{n+1},y_n + Hx_n,y_{n+1} + 4\Delta 1^2 \mu\sigma\partial Hx_n,y_n)/4. \tag{11}$$

Equations (8) and (9) can be approximated with one of the three point derivative formulas [8],

$$\partial Hx_n,y_n/\partial x \simeq (-3Hx_n,y_n + 4Hx_{n+1},y_n - Hx_{n+2},y_n)/2\Delta 1, \tag{12}$$

$$\partial Hx_n,y_n/\partial x \simeq (-Hx_{n-1},y_n + Hx_{n+1},y_n)/2\Delta 1, \tag{13}$$

$$\partial Hx_n,y_n/\partial x \simeq (Hx_{n-2},y_n - 4Hx_{n-1},y_n + 3Hx_n,y_n)/2\Delta 1. \tag{14}$$

The three point formulas were chosen because their error decreases as a function of $\Delta 1^2$ as opposed to a two-point formula whose error decreases only as a function of $\Delta 1$.

The Driving Field

The driving magnetic field for the iterative solution to the square box was assumed to be uniform to match the assumptions of the analytic method. When the derivative of the magnetic field was calculated for the bone models, the field was not considered uniform. Instead, the equations and program for the magnetic field created by a set of Helmholtz

coils were obtained from Sampsel [6]. The derivative of the magnetic field was then made proportional to the field strength at the point in question. One advantage of using the Helmholtz coils as a driving source, in addition to being more realistic, was that the boundaries perpendicular to the bone could be set in an area of small magnetic field, minimizing their effect of being "artificial boundaries" on the solution.

Implementation of the Relaxation Method in FORTRAN

A representative FORTRAN program that solves the equations for the fields inside a square box is included in Appendix A. The program assumes the driving magnetic field is uniform on the boundaries of the box with its derivative equal to BPRIME. ESTIMATE does the iterating and keeps track of the maximum change between the last two iterations with the variable EPS. When the maximum error criteria is satisfied, the program calculates the current densities at each point with the functions THEL, THER, and THEM. THEL is used to calculate the derivative when the point in question is on the left hand side of the interval, THEM is used to calculate the derivative when the point is in the middle, and THER is used to calculate it when it is on the right hand side. Thus, THEL and THER are used to calculate the current density at a boundary, and THEM is used everywhere else inside the box.

Assumptions

In most simulations there must be some assumptions to simplify the model that is used. In this case seven simplifying assumptions were made. These assumptions are listed and discussed below.

1. It was assumed the system was linear and contained

homogeneous regions.

2. It was assumed that the back emf could be ignored.

3. The conductivity of the fluid pocket and intermedullary canal were assumed to be the same as that of the flesh surrounding the bone.

4. The leg was assumed to be a cylinder with a radius of 32 mm. and a length of 300 mm., the bone was assumed to be a cylinder with a radius of 8 mm., and the intermedullary canal was assumed to be a cylinder with a radius of 4 mm. (when it was included).

5. The width of the break varied from 4 mm. to 16 mm. (i.e. one half to two bone radii).

6. The time-rate-of-change of the magnetic field was assumed to be 3.48 Tesla/second in all cases.

7. The bone was assumed to be a perfect non-conductor.

Assumption (1) was made because biological systems are normally assumed to be linear when dealing with large dimensions. Experiments dealing with low levels and dimensions that are large compared to a single cell show that this is a good approximation. Since this case deals with low frequencies and low drive levels, along with large dimensions, it is a valid assumption. It is probably not valid to make this assumption on a cellular level. At the cellular level there are processes such as active transport of ions across the cell wall, and pockets of protein "floating" in the cell wall which have nonlinear transfer characteristics. These processes make the cell a very nonlinear system.

Assumption (2) was made when the second term of equation (1) was ignored. This assumes the conductivity current term of the equation is much larger than the displacement current term. If we assume a sinusoidal time variation, then the right hand side of (1) becomes $(\sigma + j\omega\epsilon)\bar{E}$. If we assume the point where we must include the second term occurs when $|\sigma| < |10j\omega\epsilon|$, with values of σ for physiological saline (approximately 1 mho/cm) and permittivity (approximately 200), then, the frequency where we have to include the second term occurs at 56 Mhz. Since almost all of the energy in most of the signals being used presently is contained in the frequency region below 1 Mhz., the assumption appears valid in this case.

The next three assumptions were made as a matter of convenience. The conductivities of the three regions may vary slightly, but it will not change the current density pattern enough to justify the extra computer time needed to account for the small variation. The physical dimensions were chosen to be reasonably close to an average leg and bone break, yet allow for easy computer programming. The width of the break was varied to investigate the effect it has on peak current density.

Assumption (6) was made since this is the time-rate-of-change of devices presently in clinical use. If other values are desired then direct scaling can be used. For example, if the time-rate-of-change is doubled, the current density is doubled everywhere.

The last assumption was made to cut down on the time needed to arrive at a solution. The conductivity of the bone is known to be finite, and it is usually assumed to be a tensor quantity. The actual conductivity has been measured, however, and shown to be about two

orders of magnitude smaller than the conductivity of the surrounding flesh. In addition, most of the conductivity is due to saline contained in the canals permeating the bone. The outside of the bone, which is primarily mineral deposits, looks like a non-conducting boundary.

CHAPTER 3

RESULTS

Comparison Between the Two Methods

McLeod [5] has derived the analytic solution for the current density in a rectangular conducting box with a uniform magnetic field applied to it. Assuming the magnetic field is in the z direction the resulting equation for one component of the current density is:

$$J_x \simeq \frac{j\omega\mu\sigma Ho(2a)}{\pi^2} \sum_{n_{odd}} \frac{4}{n^2} [\cos((n\pi/2a)x)] \left[\frac{\sinh((n\pi/2a)y)}{\cosh((n\pi/2a)h)}\right]. \quad (15)$$

The coordinates and variables used are shown in figure 1.

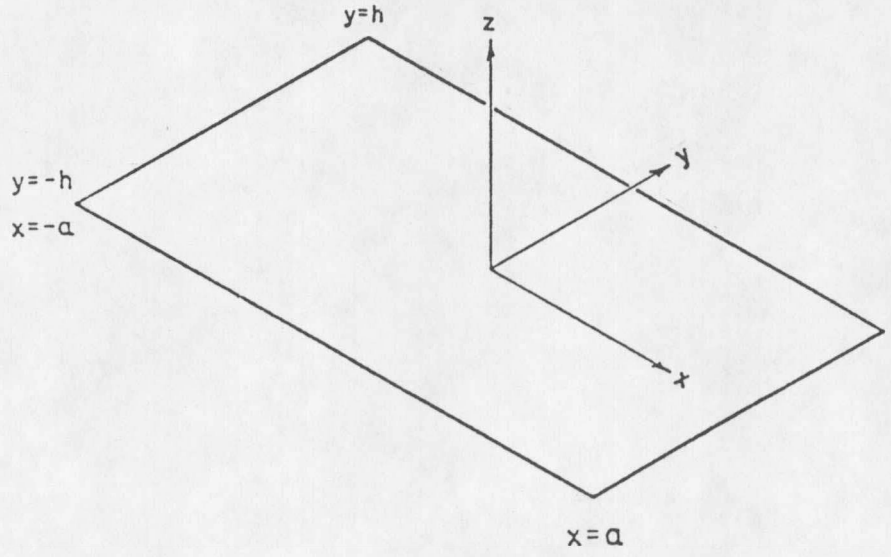

Figure 1. Coordinate system of rectangular conducting box.

The data from the Relaxation Method were compared with McLeod's analytical solution for the case of a square box. A box was chosen with the dimensions 5.25 mm. by 5.25 mm. with a conductivity of .71 mhos/cm., and a time-rate-of-change of the magnetic field of 5.3 Tesla/sec. This yielded a 43 by 43 grid with a spacing of .125 mm. in both directions. The driving parameters of the coil were chosen to be similar to ones now in clinical use. The comparison between the two yielded very similar results. For the analytic solution, the peak values of J_x, J_y, and the total magnitude were all .66722 microamps/cm^2, and for Relaxation Method they were 0.66618 microamps/cm^2. The maximum difference between the two methods was .01005 microamps/cm^2 (1.50% of the maximum value), with an average difference of $4.6 * 10^{-9}$ ($6.9*10^{-7}$%) for J_x and J_y, and $2.6*10^{-5}$ (.0039%) for the total magnitude. Finally, the correlation between the two methods was .9999968 for J_x and J_y, and 0.9999775 for the total magnitude. This clearly shows that both methods are converging to the same values. The difference can be attributed primarily to the numerical approximations made while calculating the spatial derivative of Hz.

Presentation of the Data for the Square Box Example

One of the problems encountered is how to present the data to researchers in different disciplines. A printout of an array of numbers is difficult to interpret. To further complicate matters the data are two-dimensional (J_x,J_y) over a two-dimensional area (the dimensions of the box). A combination of four methods were used to solve this problem.

The first method used to present the data is a "flow map" of the

system. At each point in the grid a short line segment is drawn whose length is proportional to the magnitude of the current density and whose direction indicates the direction of current flow. Figure 2 is an example of this method for the square box. This picture shows how the current density starts out at 0 in the center and increases to a maximum at the edge of the box. It also shows how the current tends to flow in a circle in the center and parallel to the boundaries at the edges.

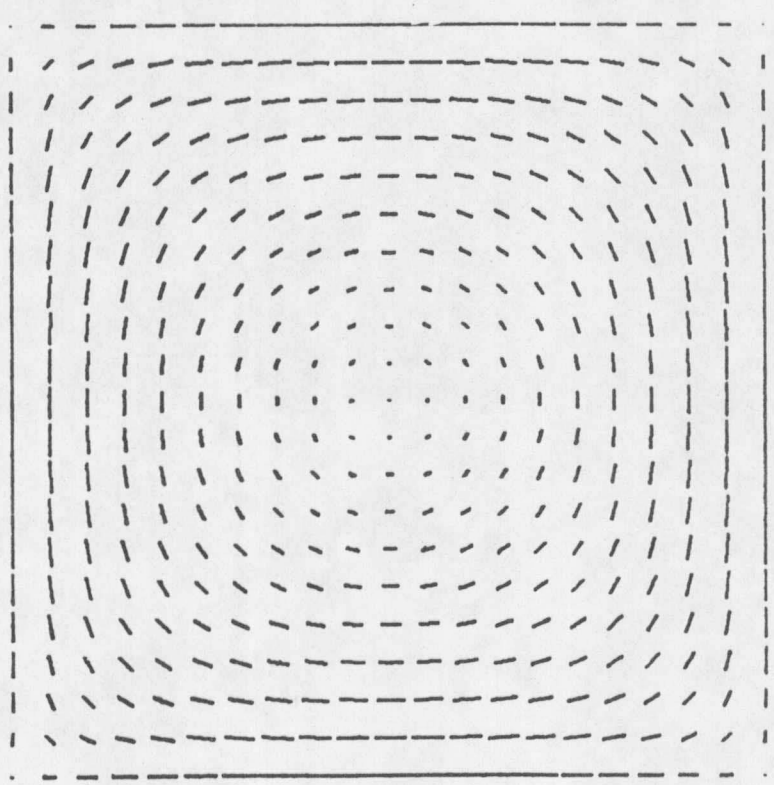

Figure 2. Magnitude and Flow Graph of Square Box

The second method is very similar to the first. The magnitude information is taken out by making the line segments all the same length. This brings out the current flow patterns in areas where the current density is small. Figure 3 gives us an example of this. One can see the direction of flow more clearly in the center now.

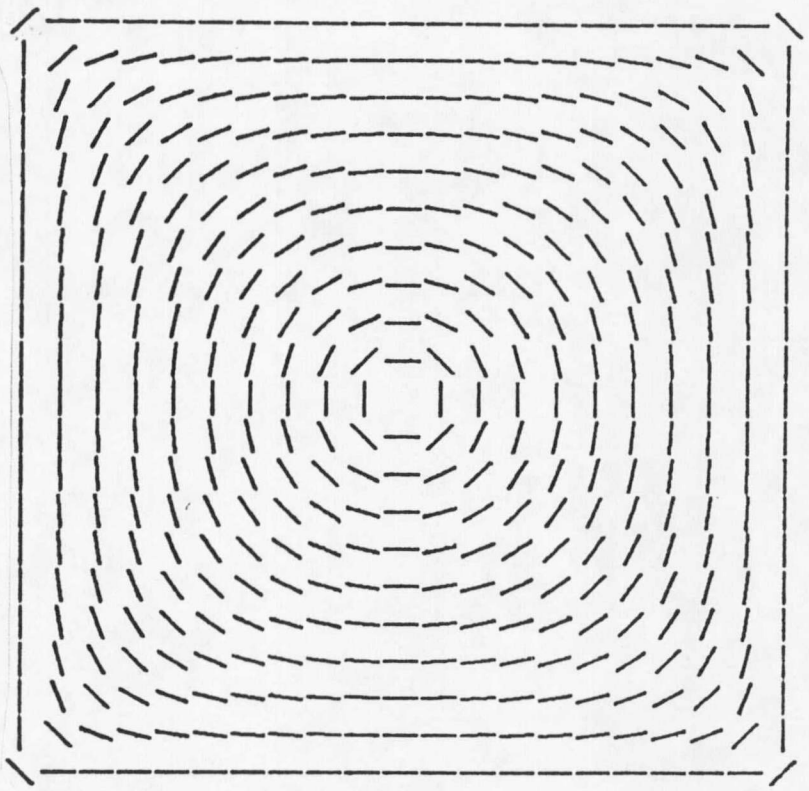

Figure 3. Flow Graph of Square Box.

Method three contains only magnitude information about the current density. The magnitude of the current density is plotted as the vertical dimension in a three dimensional picture. This gives the viewer a good idea of what is happening spatially in the system. Figures 4 through 7 are some representative three dimensional views of the square box as the observer "walks" around the box. Figure 4 is a view of the current density over the whole box. The thin lines are the actual grid points shown in the plane of 0 magnitude. This view clearly shows that the magnitude is 0 in the center of the box and at the corners, and that the maximums are at the center of the edges of the box. This view also indicates that even for this simple geometry, the spatial current distribution is not a simple function. Figures 5, 6, and 7 are

different views of one quadrant of the box. The insets show the direction of observation.

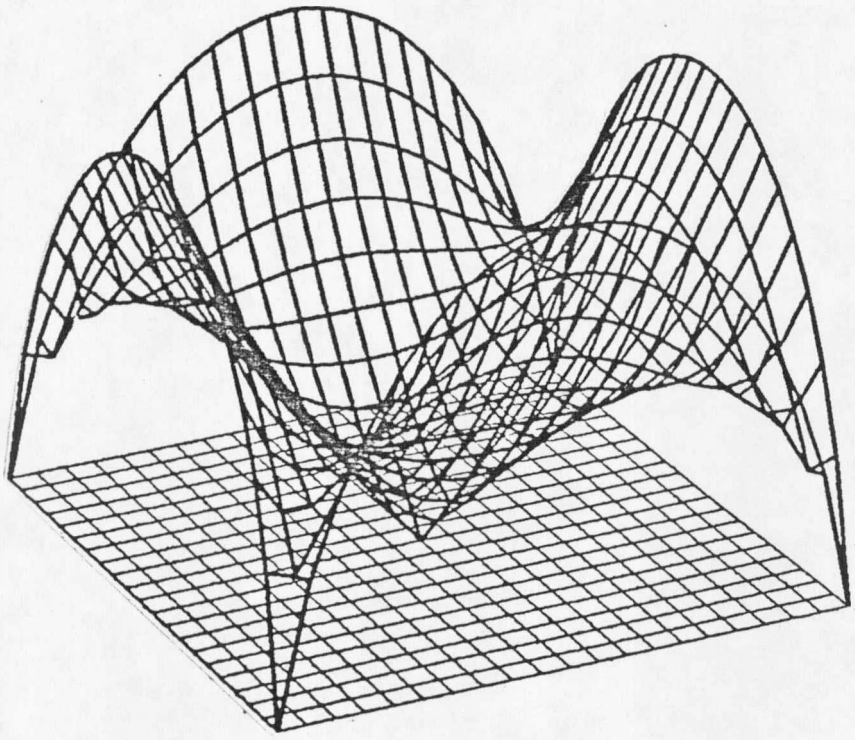

Figure 4. Three Dimensional View of Square Box .

The last method is just a normal X-Y plot of the magnitude of current density along some line of interest. Figures 8, 9, and 10 show representative graphs of this method. The characteristic shapes shown in these graphs can also be seen in the three dimensional views. This gives the observer a connection between the different methods of presentation.

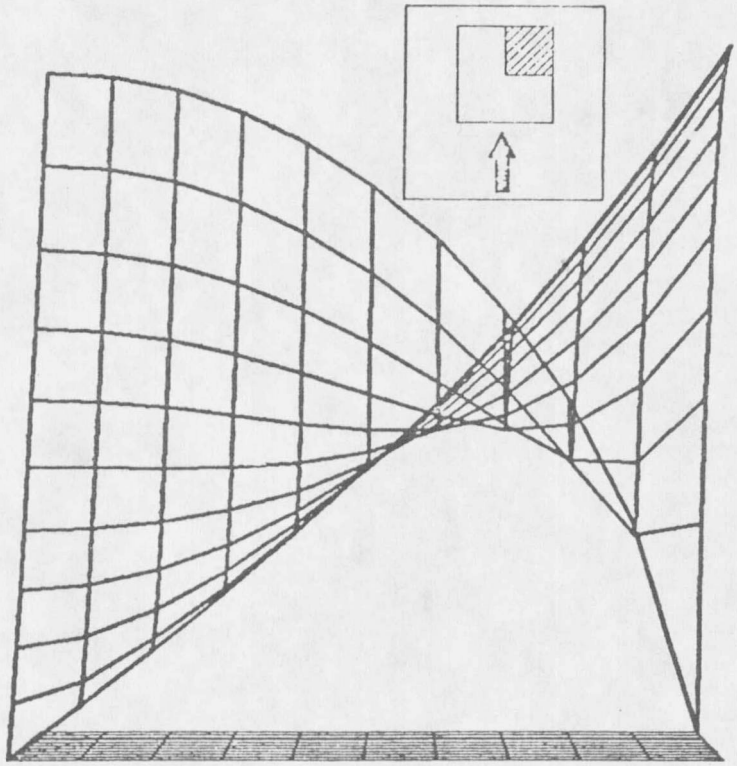

Figure 5. Three dimensional View of Square Box from the Edge

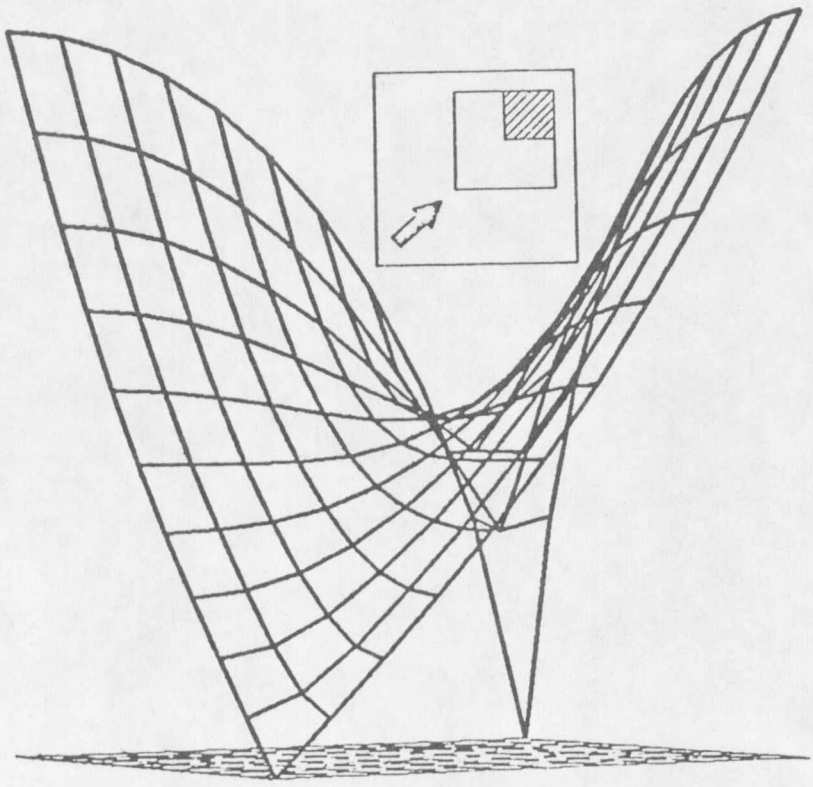

Figure 6. Three Dimensional view of Square Box from Inside Corner

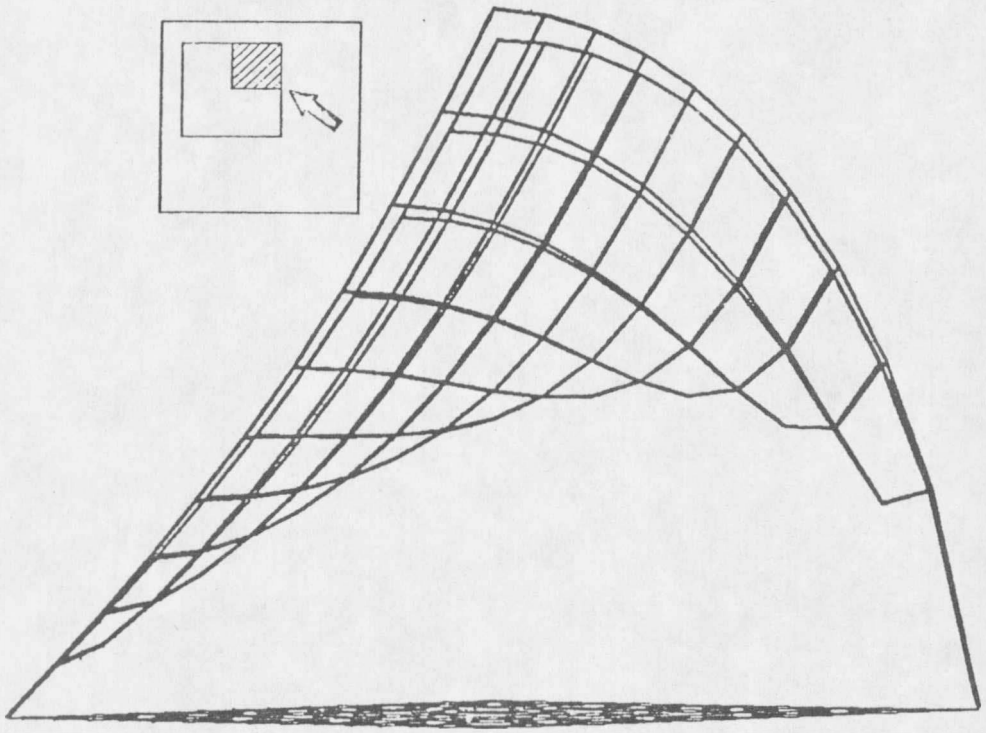

Figure 7. Three dimensional view of Square Box from Outside Corner

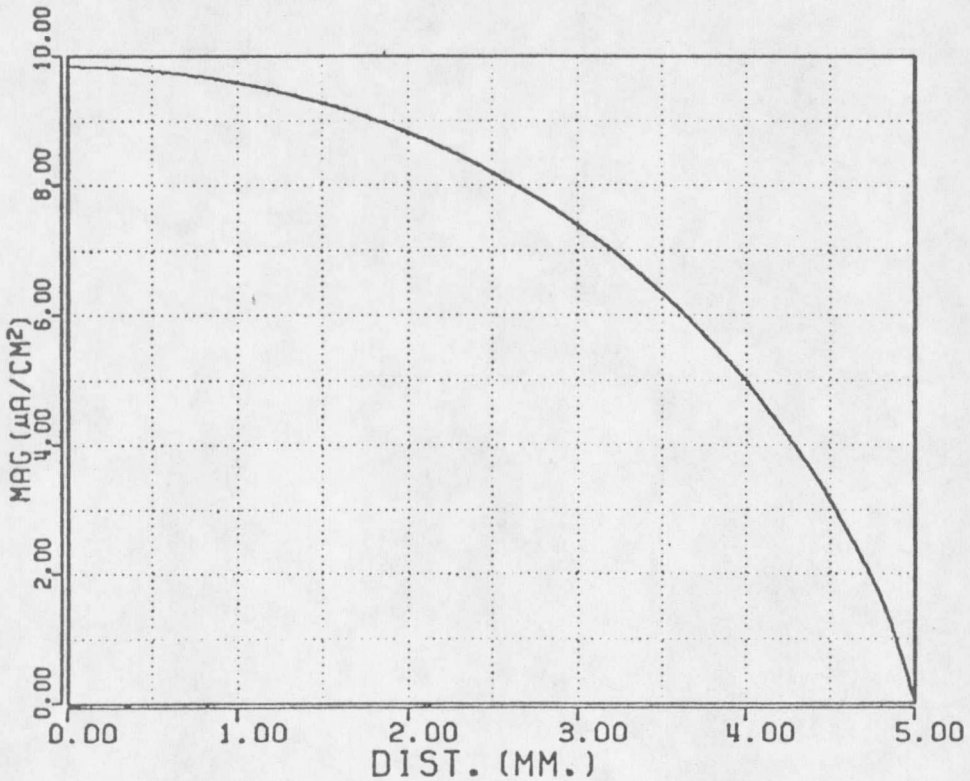

Figure 8. Graph of Magnitude of Current Density along the Edge of the Square Box

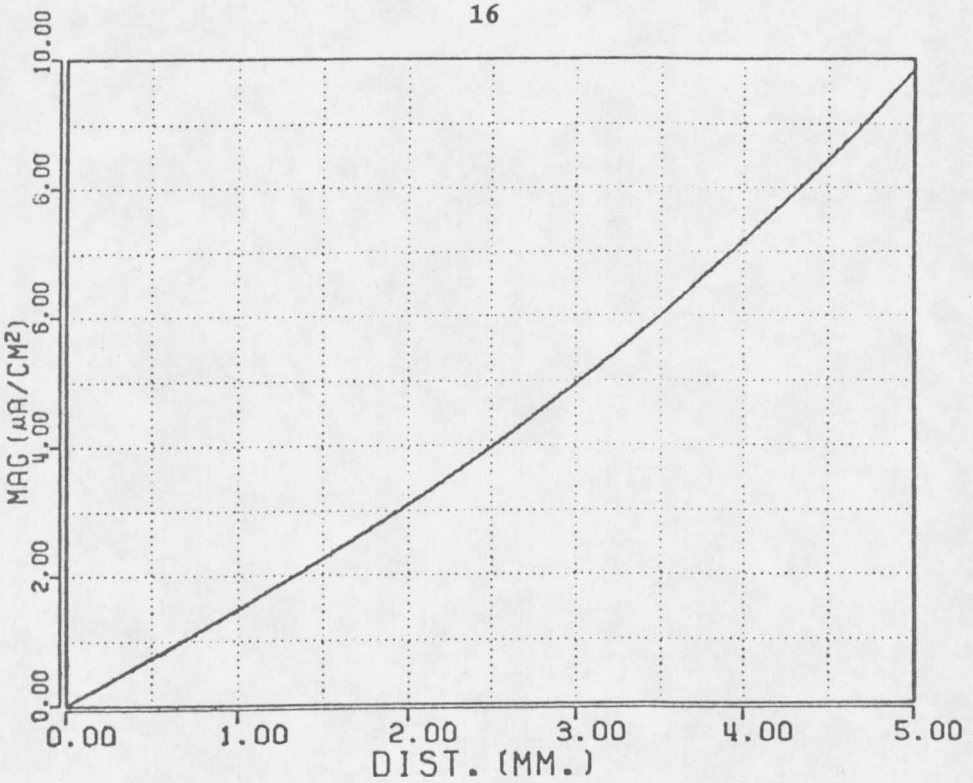

Figure 9. Magnitude of Current Density along the Centerline of the Square Box.

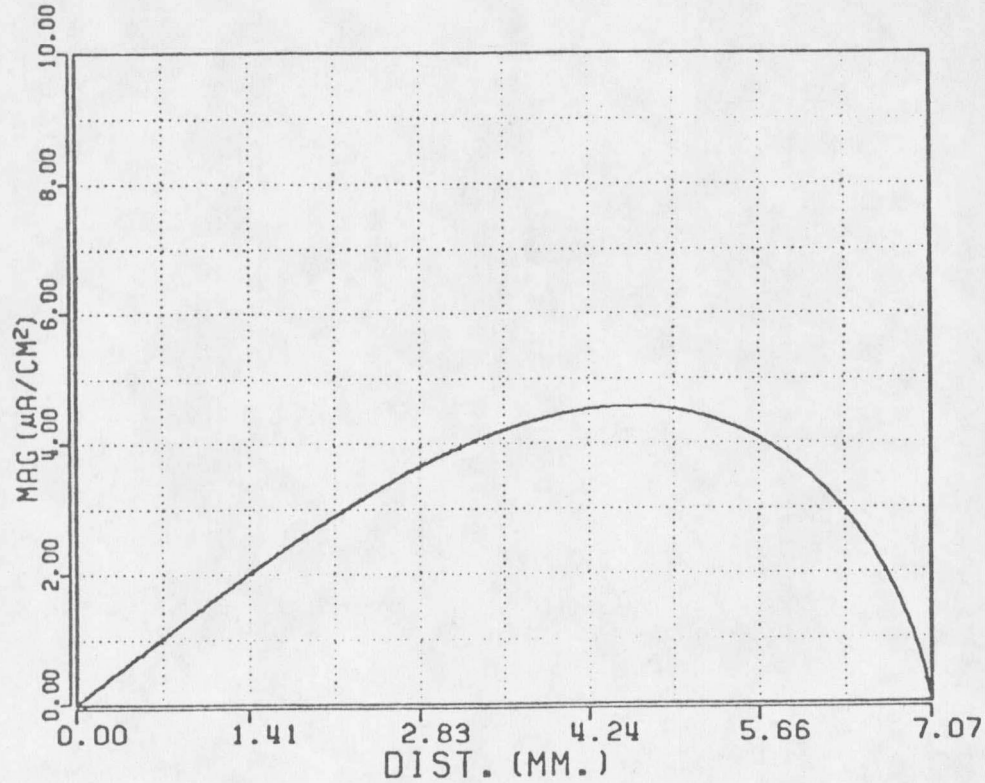

Figure 10. Graph of the Magnitude of Current Density along the Diagonal of the Square Box.

The Bone Models

The diagrams of the different bone model boundaries are included in Appendix C. They are meant to represent a cross-section of a leg taken along the longitudinal center line. Most of the models were chosen to to be symmetric about the longitudinal center line in order to reduce the computer time needed to find a solution and simplify the presentation of the data.

Since the dimensions of the systems are all similar, any differences in peak induced current density between them can be attributed to differing boundary conditions. In these models there are three types of breaks, male, female, and square. The female has the sharpest "point", the square break has an intermediate point, and the male has the dullest point. Since the peak current density seems to occur at these points, it would seem to be a good place to compare current densities. In the case of the female point, the current density was 13.7 microamps/cm^2, the square point was 10.5 microamps/cm^2, and the male point was 8.7 microamps/cm^2. This gives us a difference in magnitude of 1.57:1 which could be significant. If the electric current is the coupling mechanism to the cell, then the external drive level could be sharply reduced if the coils were positioned to take advantage of an abrupt point.

In addition to boundaries, the separation of the two bones has an effect on the peak current density. Figures 12-14 show the same fracture with the ends separated by different distances. For a separation of 4 mm., the peak current density was 6.5 microamps/cm^2, for 8 mm. it was 8.6 microamps/cm^2, and for 16 mm. it was 11.5 microamps/cm^2. Notice that the current density increases in a nonlinear fashion as the ends of

the bones become more separated. This may be either good or bad. If the biological effect has a dose or amplitude window as some people suggest, the effect may be greater if the separation is increased for a given drive level. If the drive level is great enough, however, the effect may diminish for a greater separation. The bone also appears to have a harder time healing itself if the separation is too large.

Appendix D contains all of the flow and magnitude graphs of the bone models. The data are shown for only one quadrant of the break, but the data for the other quadrants are a mirror image of the quadrant shown. The first fact that becomes apparent when looking at the flow graphs is that the current tends to flow parallel to the bone. The magnitude graphs also show the current density is much larger at the corners of the bone than the rest of the system. As the point of the bone becomes more acute (more pointed), the current density tends to increase to a higher value and become more localized. As the distance between the bone faces increases, the peak current density increases in a nonlinear fashion. Let us take a closer look at one example, the model that has two female type of bone faces with the intermedullary canal included. Figures 18 and 19 clearly demonstrate that the current does tend to stay parallel when it is close to the bone. Along the face of the bone, however, the lines begin to pull away since they must also continue on to the other side of the break, and finally back to flowing parallel to the other portion of the bone. An interesting secondary feature appeares on the bone face at approximately the center. This is an induced current minimum. This feature is dependent on the boundaries of the system. In the case of the square end

boundaries, the minimum doesn't exist.

The flow and magnitude graphs give a good overall view of how the system looks, but it does not give the actual levels of induced current, or even a good idea of how the magnitude changes in the region of the break. The X-Y plots in Appendix E give a much better idea of the actual magnitude of the current inside the break. Figure 32 shows the magnitude of current density versus distance for the centerline between the ends of the break. Figure 33 shows a parallel slice containing the outside point of the bone. Notice how much the current density varies near the point. We expected to see this from the magnitude and flow graphs shown previously.

The next graph shows a slice taken near the induced current minimum. The bone shows up as the area with zero current density since it is a perfect non-conductor. Figure 35 shows a slice containing the point on the inside of the break. Notice again that a smaller current maximum occurs at the point. These graphs distinctly point out the non-uniform nature of the current density. One can also see that the edge of the bone tends to be the current maximum for that area. This is one advantage of using inductive coupling. The maximum induced current density is located at the break, so theoretically you can localize the induced current in the areas where it is needed.

Appendix F contains the three dimensional views of the break. The views start looking at the outside of the bone with the break to the left. Each proceeding view moves around 45 degrees clockwise to give the viewer a good perspective of all sides. Each of the features shown in the previous graphs can be located in these three dimensional views.

These views again point out how the current density is maximized at the points. The difference is so great on the outside point that it makes a good landmark in viewing the different graphs. Figure 41 shows several features very well. The observer is standing in the break looking down the bone. The main point can be seen on the right hand side of the view and the lesser point to the left. The current is seen decreasing as one moves away from both edges of the bone, also, the minimum on the bone face can be seen. There appears to be an "artificial boundary" extending from the inside edge of the bone into to the gap. This also appears in the two-dimensional plots as a feature at approximately 4 mm. in each of the slices (figures 32-34). Figure 45 is the view looking toward the break from inside the bone. The bone is clearly seen here along with the minimum on the bone face. Both peaks are also visible. The combination of the above methods gives the observer a good feel for the spatial distribution of the induced current density inside the break.

CHAPTER 4

CONCLUSIONS

This paper has considered a computer generated solution to the classic Helmholtz equation for several sets of boundaries. The delivery system for the square box was chosen to be a uniform magnetic field. The equations for a set of Helmholtz coils were used with the bone models to more closely approximate what researchers are using in ongoing experiments. The results from these simulations indicate that the induced current density is a strong function of the boundaries of the system. This indicates that the design of a particular delivery system may have to include spatial characteristics of the fracture in addition to the time varying parameters of the signal.

Part of the problem with the computer solution is presenting the data in fashion that is straightforward and simple so that it is usable by a wide variety of researchers in multi-disciplinary fields. This point has been addressed by displaying the data in several different forms, and shows that a connection between the different forms can be seen.

The bone models that were chosen simulate simple non-union fractures in the lower leg. One of the first conclusions that can be drawn is that the current density is far from uniform. In fact, it appears that as much as an order of magnitude variation can be seen in relatively confined areas. If we assume that it is the current density and not the magnetic field that stimulates the bone to heal, then the peaks of

current density occurring at the points of the bone may be of prime interest. Also, if there is a "window" of current density above or below which the stimulation is not effective or even harmful, then the spatial distribution of the current density becomes important to both the designers of the delivery system, and how the unit is placed around the break.

Another conclusion that can be drawn from the data is that the general flow of the current density lines is not across the gap. Rather the flow tends to be parallel to the bone until points relatively far from the bone are reached. Even in the gap the lines tend to loop into and back out of the gap as opposed to flowing across the gap.

The limitations of this model should also be pointed out. First and probably most importantly the computer time (and cost) increases very rapidly as the model becomes more complex. This limits the model's usefulness in simulating breaks that are more realistic. However, adding more points and bends would be very expensive to do and would not yield much more useful information. One can also decrease the grid size for more accuracy and better resolution, but again, the computer time increases dramatically even when the resolution is just doubled.

In summary, this thesis presents a tool to help researchers better understand the underlying mechanisms in their systems. Its use for real fractures is limited, but it should give researchers a better feel for what is happening in their system. Simulations such as this one will become increasingly vital as the search for a mechanism narrows down to the cellular level.

REFERENCES CITED

REFERENCES CITED

1. Smith, S. D., and Feola, J. M., "Pulsed Magnetic Field Modulation of LSA Tumors in Mice," Journal of Bioelectricity, Vol. 1, 1982, pp. 207-229

2. Christel, P., Cerf, G., and Pilla, A. A., "Modulation of Rat Radial Osteotomy Repair Using Electromagnetic Current Induction", Mechanisms of Growth Control, Ed. R. Becker, C. C. Thomas Press, New York, 1981

3. Sisken, B. F., Fowler, I., Kryscio, R., "The Effects of Pulsed Electromagnetic Fields (PEMF) on Chick Embroys After Limb Amputation.", Presented at the 5th Annual Session of the Bioelectromagnetics Society, June 12-17, 1983

4. Trillo, M. A., Jimenez, M. A., Leal, J., Ubeda, A., and Delgado, J. M. R., "Alterations and Fractional Recovery of Chick Embroys Exposed to Electromagnetic Fields.", Presented at the 3rd Annual Meeting of the Bioelectrical Repair and Growth Society, October 2-5, 1983

5. McLeod, B. R., Pilla, A. A., Sampsel, M. W., "Electromagnetic Fields Induced by Helmholtz Aiding Coils Inside Saline Filled Boundaries", Bioelectromagnetics, Vol. 4, Num. 4, 1983

6. Sampsel, M. W., "Experimental Investigation of Electromagnetic Fields from Helmholtz Type Circular Coils", Master's Thesis, Montana State University, June, 1982

7. Southwell, R. V., Relaxation Methods in Theoretical Physics, Oxford at the Claredon Press, 1946, pp. 1-66

8. Burden, R. L., Faires, J. D., Reynolds, A. C., Numerical Analysis, Prindle, Weber, and Schmidt, 1978, pp. 172-186

APPENDICES

APPENDIX A

SQUAREBOX PROGRAM

APPENDIX A

SQUAREBOX PROGRAM

```
C*************************************************************************
C***  THIS PROGRAM CALCULATES THE CURRENT DENSITY INSIDE A SQUARE      ***
C***       CONDUCTING BOX WITH DIMENSIONS 5.25 mm. by 5.25 mm.         ***
C*************************************************************************
C***                                                                   ***
C***  Variables:                                                       ***
C***     GRID: Grid is a two-dimensional matrix containing the         ***
C***           values of the H field in the box.                       ***
C***     BPRIME: Bprime is the time derivative of the driving B        ***
C***             field.                                                ***
C***     SIGMA: Sigma is the conductivity of the box.                  ***
C***     EPS:  Eps contains the largest change in grid between the     ***
C***           last two iterations.                                    ***
C***     EPSMIN: Epsmin contains the maximum allowed change between    ***
C***             any two iterations before the program will cal-       ***
C***             culate the current densities inside the box.          ***
C***     CUR: Cur conatains the current densities inside the box.      ***
C***     MAX: Max is the maximum number of iterations.                 ***
C***                                                                   ***
C*************************************************************************
C***  Subprograms:                                                     ***
C***     ESTIMATE: Estimate uses the Relaxation Method to calculate    ***
C***               the next point in an iteration.                     ***
C***     THEL: Thel calculates the derivative with a three point       ***
C***           method assuming the point in question is on the         ***
C***           left hand side.                                         ***
C***     THEM: Them calculates the derivative with a three point       ***
C***           method assuming the point in question is in the         ***
C***           middle.                                                 ***
C***     THER: Ther calculates the derivative with a three point       ***
C***           method assuming the point in question is on the         ***
C***           right hand side.                                        ***
C***                                                                   ***
C*************************************************************************
      IMPLICIT REAL*8 (A-H),(L-Z)
      REAL*8 GRID(-21:21,-21:21)
      REAL*8 EPS,BPRIME,SIGMA
      REAL CUR(-21:21,-21:21,2)
      REAL*8 EPSMIN
      WRITE(5,4)
```

```
C*********************************************
C******** Input magnetic field derivative, conductivity,
C******** maximum change between two iterations, and
C******** maximum number of iterations.
C*********************************************
 4    FORMAT(' What are Bprime,sigma, epsilon, and the maximum # of '
     1    ,'iterations? ')
      READ(4,*)BPRIME,SIGMA,EPSMIN,MAX
      BPRIME=BPRIME*SIGMA*.125D-3*.125D-3
      EPS=2.*EPSMIN
      DO 8 II=1,MAX
C*********************************************
C******** Check for change between two iterations and branch out if
C******** the criteria is satisfied.
C*********************************************
      IF (EPS.LT.EPSMIN) GOTO 8
      EPS=0.
C*********************************************
C******** Do the relaxation method.
C*********************************************
      CALL ESTIMATE(-20,20,1,-20,20,1,5,GRID,EPS,BPRIME)
      CALL ESTIMATE(20,-20,-1,20,-20,-1,5,GRID,EPS,BPRIME)
      WRITE(5,*)II,EPS
 8    CONTINUE
C*********************************************
C******** Calculate the current on the edges of the boxes.
C*********************************************
      DO 9 J=-20,20
      CUR(J,-21,1)=8D5*THEL(GRID,J,-21,0,1)
      CUR(J,-21,2)=0.
      CUR(J,21,1)=8D5*THER(GRID,J,21,0,1)
      CUR(J,21,2)=0.
      CUR(-21,J,2)=8D5*THEL(GRID,-21,J,1,0)
      CUR(-21,J,1)=0.
      CUR(21,J,2)=8D5*THER(GRID,21,J,1,0)
 9    CUR(21,J,1)=0.
C*********************************************
C******** Calculate the current inside the box.
C*********************************************
      DO 45 I=-20,20
      DO 44 J=-20,20
      CUR(I,J,1)=8D5*THEM(GRID,I,J,0,1)
      CUR(I,J,2)=8D5*THEM(GRID,I,J,1,0)
 44   CONTINUE
 45   CONTINUE
C*********************************************
C******** Print out the results of the run.
C*********************************************
      WRITE(6,*)((CUR(I,J,1),J=-21,21),I=-21,21)
      WRITE(6,*)((CUR(I,J,2),J=-21,21),I=-21,21)
      END
```

```
C*********************************************
C******** Estimate
C*********************************************
      SUBROUTINE ESTIMATE(YSTART,YEND,DELTAY,XSTART,XEND,DELTAX,N,
     1    GRID,EPSILON,BPRIME)
      IMPLICIT INTEGER (A-Z)
      REAL*8 GRID(-21:21,-21:21),EPSILON,OLD,BPRIME
      TEMP=DFLOTJ(DELTAY*DELTAX)
      DX=ABS(DELTAX)
      DY=ABS(DELTAY)
      DO 10 J=1,N
           DO 20 JVERT=YSTART,YEND,DELTAY
                DO 30 JHORZ=XSTART,XEND,DELTAX
                 OLD=GRID(JVERT,JHORZ)
                 GRID(JVERT,JHORZ)=(GRID(JVERT-DX,JHORZ)+
     1                             GRID(JVERT+DX,JHORZ)+
     1                             GRID(JVERT,JHORZ-DY)+
     1                             GRID(JVERT,JHORZ+DY)-
     1                             BPRIME)/4D0
                 IF(EPSILON.LT.DABS(GRID(JVERT,JHORZ))-
     1                DABS(OLD)) EPSILON=DABS(DABS(GRID(JVERT,JHORZ))-
     1                DABS(OLD))
 30             CONTINUE
 20        CONTINUE
 10   CONTINUE
      RETURN
      END
C*********************************************
C******** Thel
C*********************************************
      FUNCTION THEL(F,X,Y,DX,DY)
      REAL*8 F(-21:21,-21:21)
      INTEGER X,Y,DX,DY
      THEL=-3.*F(X,Y)+4.*F(X+DX,Y+DY)-F(X+2*DX,Y+2*DY)
      THEL=THEL/2.
      RETURN
      END
C*********************************************
C******** Them
C*********************************************
      FUNCTION THEM(F,X,Y,DX,DY)
      REAL*8 F(-21:21,-21:21)
      INTEGER X,Y,DX,DY
      THEM=-F(X-DX,Y-DY)+F(X+DX,Y+DY)
      THEM=THEM/2.
      RETURN
      END
```

```
C*********************************************
C******** Ther
C*********************************************
      FUNCTION THER(F,X,Y,DX,DY)
      REAL*8 F(-21:21,-21:21)
      INTEGER X,Y,DX,DY
      THER=F(X-2*DX,Y-2*DY)-4.*F(X-DX,Y-DY)+3.*F(X,Y)
      THER=THER/2.
      RETURN
      END
```

APPENDIX B

ANALYTIC PROGRAM

APPENDIX B

ANALYTIC PROGRAM

```
C*************************************************************************
C*** THIS PROGRAM CALCULATES THE CURRENT DENSITIES IN A RECTANGULAR ***
C***    BOX FOR A 43 BY 43 GRID USING MCLEODS ANALYTICAL METHOD.    ***
C*************************************************************************
C***                                                                   ***
C***  Variables:                                                       ***
C***     BPRIME: Bprime is the derivative of the driving B field.      ***
C***     SIGMA: Sigma is the conductivity of the box.                  ***
C***     CUR: Cur conatains the current densities inside the box.      ***
C***     HEIGHT: Height is the height of the box.                      ***
C***     WIDTH: Width is the width of the box.                         ***
C***                                                                   ***
C*************************************************************************
C***  Subprograms:                                                     ***
C***     J: J calculates the current density given the position of     ***
C***         the point in question and parameters of the box.          ***
C***     SINH: Sinh calculates the hyperbolic sine.                    ***
C***     COSH: Cosh calculates the hyperbolic cossine.                 ***
C***                                                                   ***
C*************************************************************************
4     REAL HEIGHT,WIDTH,OMEGA,SIGMA,BPRIME
      REAL VERT(5000),J,JX,JY,CUR(-21:21,-21:21,2)
      EXTERNAL J
C*********************************************
C******* Input box dimensions, conductivity, and the magnetic field
C*******  derivative.
C*********************************************
      WRITE(5,*)' Box height(mm), width(mm), cond., and Bprime?'
      READ(7,*)HEIGHT,WIDTH,SIGMA,BPRIME
      HEIGHT=HEIGHT/1000.
      WIDTH=WIDTH/1000.
      TEMP=SIGMA*BPRIME
C*********************************************
C******* Set up do loop to calculate current densities
C*********************************************
      DO 10 IX=-21,21
      DO 10 IY=-21,21
      X=IX*HEIGHT/42.
      Y=IY*WIDTH/42.
```

```
C*********************************************
C******* Calculate Jx
C*********************************************
      CUR(IX,IY,1)=J(WIDTH,HEIGHT,Y,X,TEMP)*100
C*********************************************
C******* Calculate Jy
C*********************************************
      CUR(IX,IY,2)=-J(HEIGHT,WIDTH,X,Y,TEMP)*100
 10   CONTINUE
C*********************************************
C******* Print out the results
C*********************************************
      WRITE(6,*)((CUR(IX,IY,1),IY=-21,21),IX=-21,21)
      WRITE(6,*)((CUR(IX,IY,2),IY=-21,21),IX=-21,21)
 8    FORMAT(2(X,E16.9))
      END
C*********************************************
C******** J
C*********************************************
      REAL FUNCTION J(H,W,X,Y,T)
      REAL H,W,X,Y,T
      EXTERNAL SINH,COSH
      PI=3.1415926
      YY=-1
      YT=0
      DO 10 I=1,400,2
      YY=-YY
      TEMP=FLOAT(I)*PI/W
      T1=TEMP*X
      T2=TEMP*H/2.
C*********************************************
C******* Don't allow the EXP funcion to overflow or underflow
C*********************************************
      IF (ABS(T1).GT.80.OR.ABS(T2).GT.80) GOTO 11
 10   YT=YT+YY*COS(TEMP*Y)*(SINH(T1)/COSH(T2))/(FLOAT(I)*FLOAT(I))
 11   J=YT*T*4.*W/(PI*PI)
      RETURN
      END
C*********************************************
C******** Sinh
C*********************************************
      SINH=(EXP(X)-EXP(-X))/2.
      RETURN
      END
C*********************************************
C******** Cosh
C*********************************************
      FUNCTION COSH(X)
      COSH=(EXP(X)+EXP(-X))/2.
      RETURN
      END
```

APPENDIX C

DIAGRAMS OF THE DIFFERENT BONE MODELS

APPENDIX C

DIAGRAMS OF THE DIFFERENT BONE MODELS

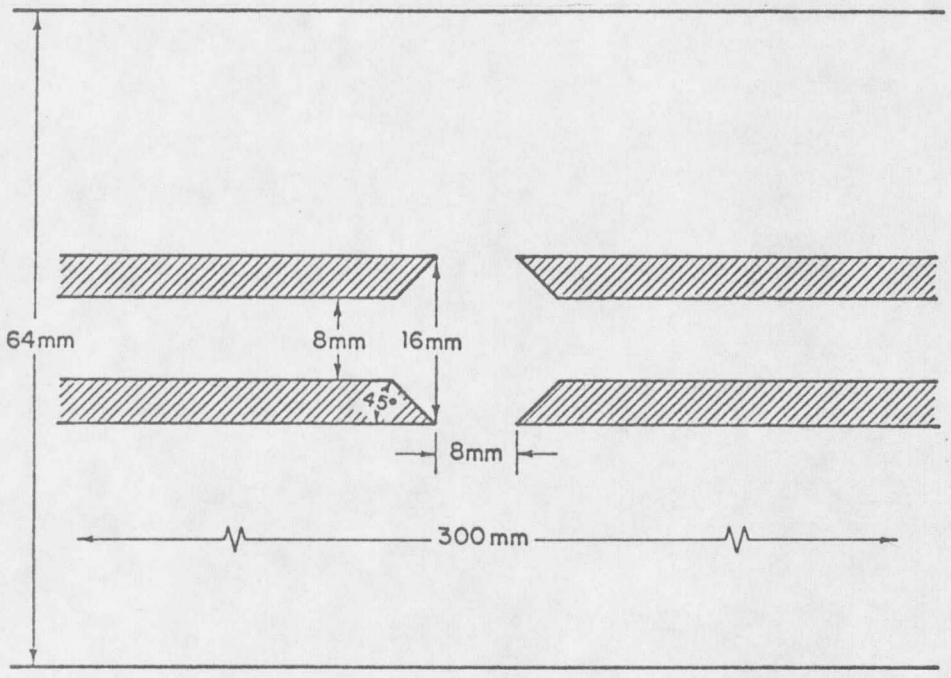

Figure 11. Diagram of Female-Female Break with I.M. Canal

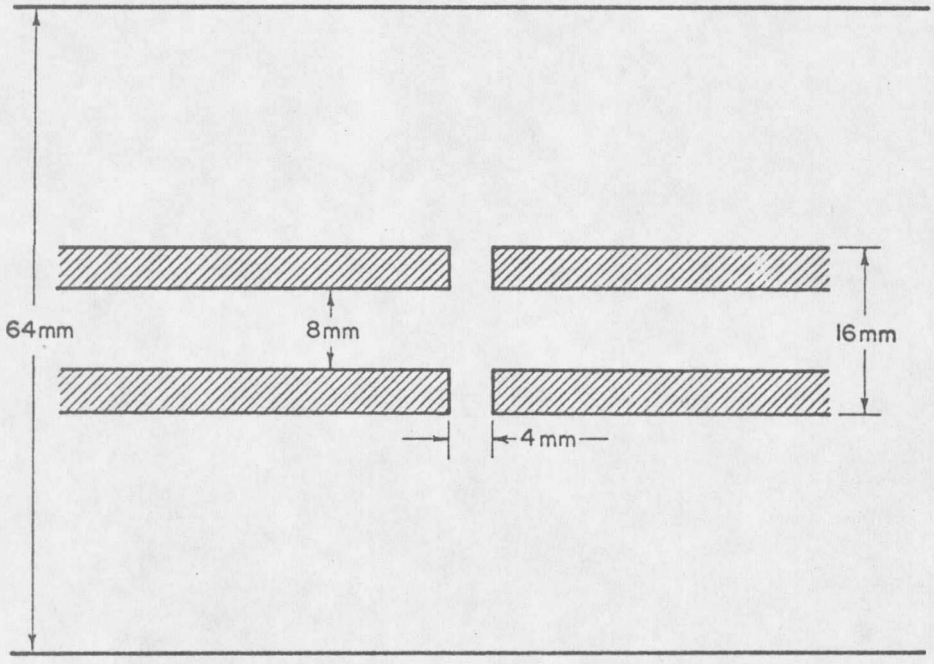

Figure 12. Diagram of Square Break with I.M. Canal (4 mm.)

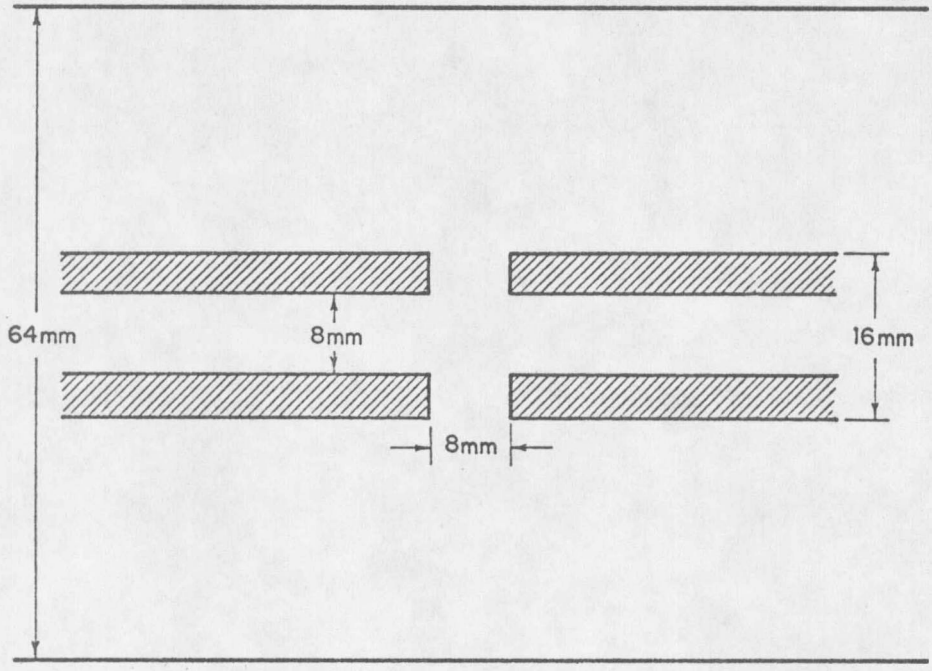

Figure 13. Diagram of Square Break with I.M. Canal (8 mm.)

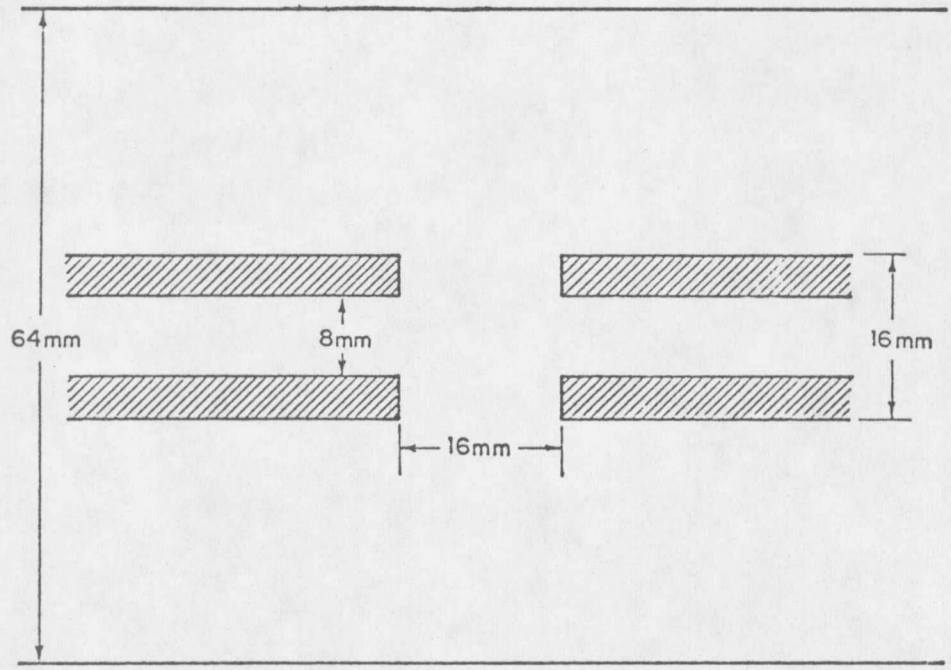

Figure 14. Diagram of Square Break with I.M. Canal (16 mm.)

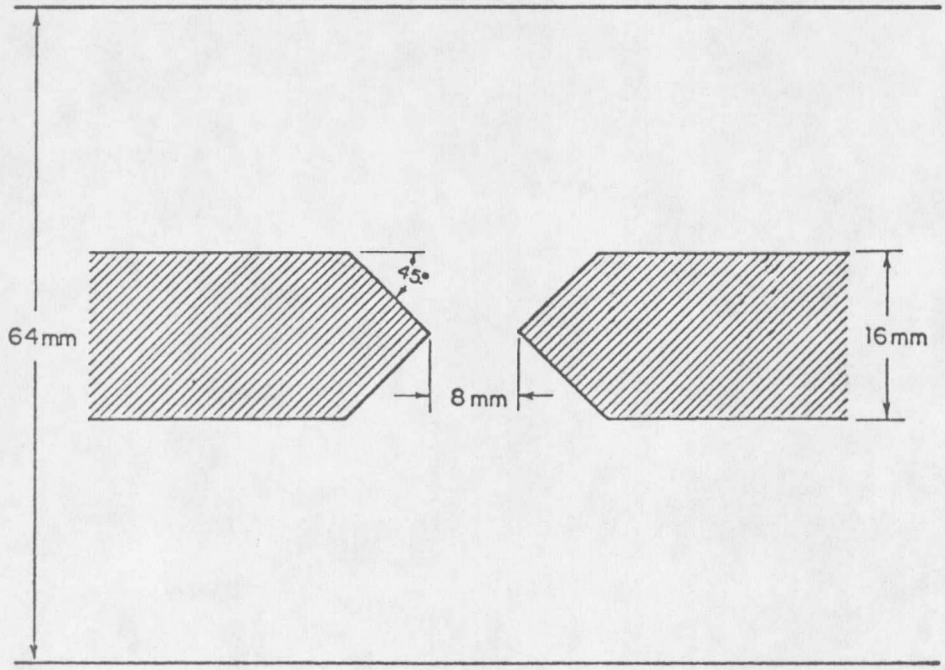

Figure 15. Diagram of Male-Male break

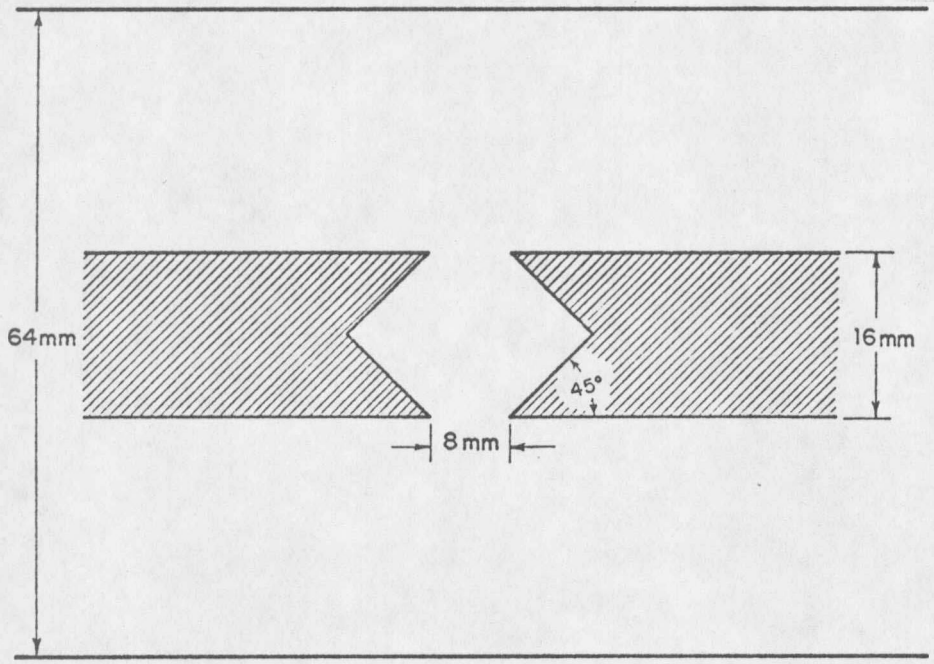

Figure 16. Diagram of Female-Female Break

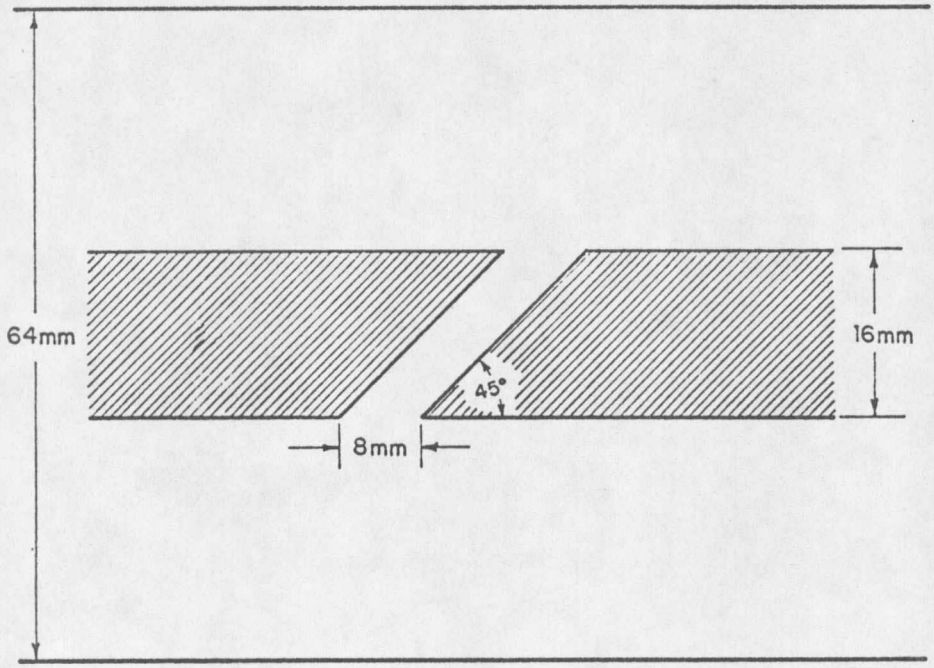

Figure 17. Diagram of Slanted Break

APPENDIX D

FLOW AND MAGNITUDE GRAPHS OF THE SPATIAL CURRENT DENSITY FOR THE BONE BREAK MODELS

APPENDIX D

FLOW AND MAGNITUDE GRAPHS OF THE SPATIAL CURRENT DENSITY FOR THE BONE BREAK MODELS

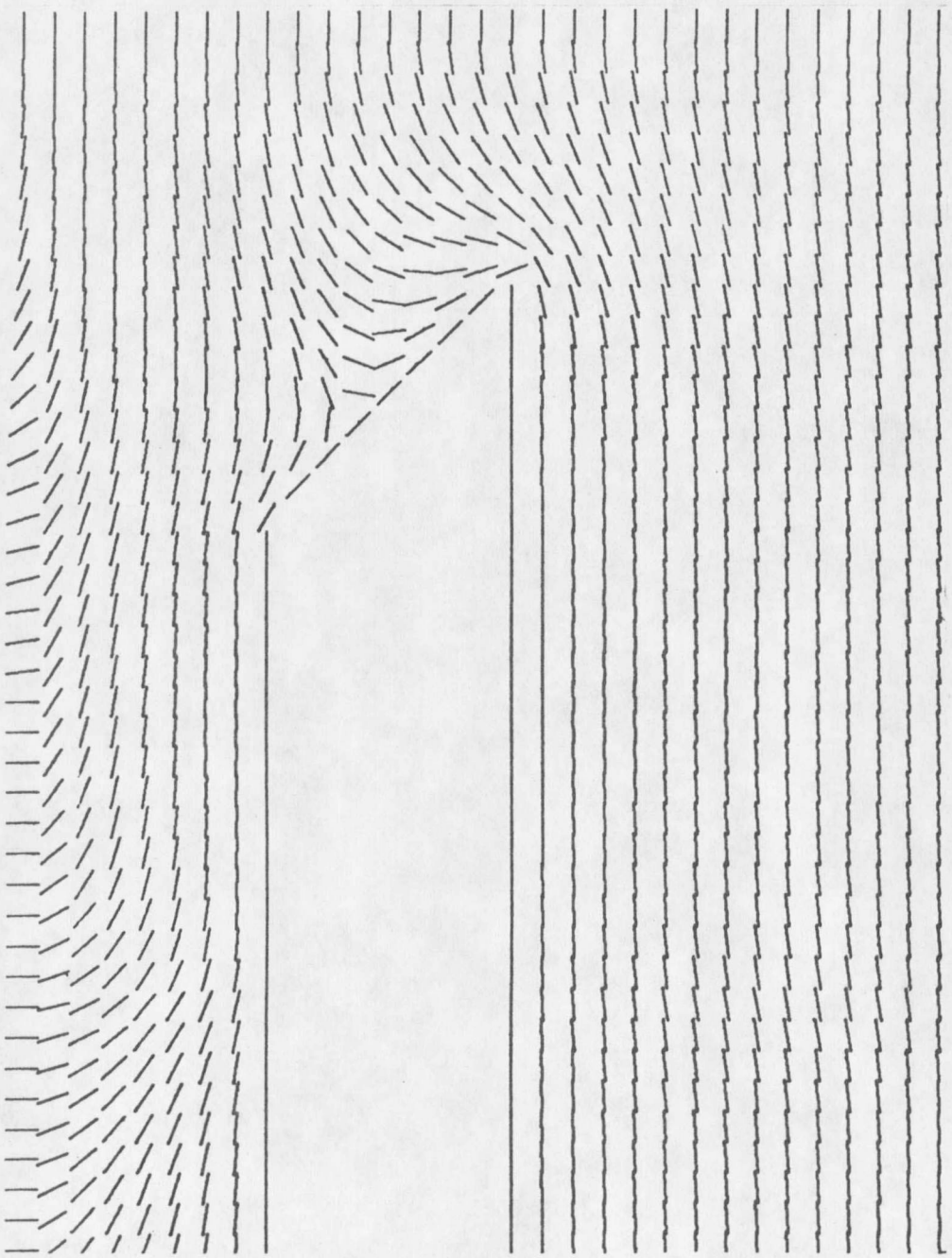

Figure 18. Flow Graph of Female-Female Break with I.M. Canal

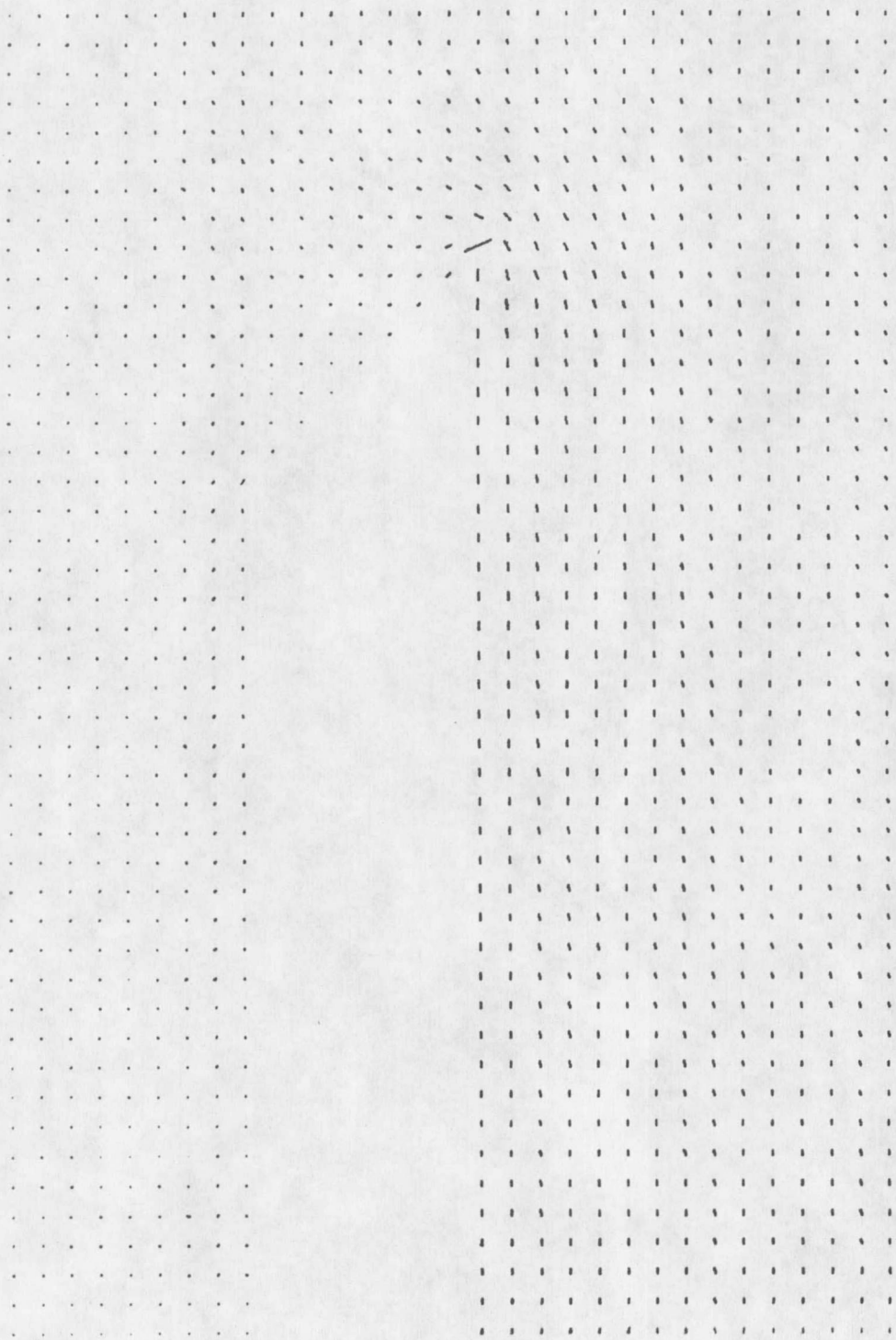

Figure 19. Magnitude and Flow Graph of
Female-Female Break with I.M. Canal

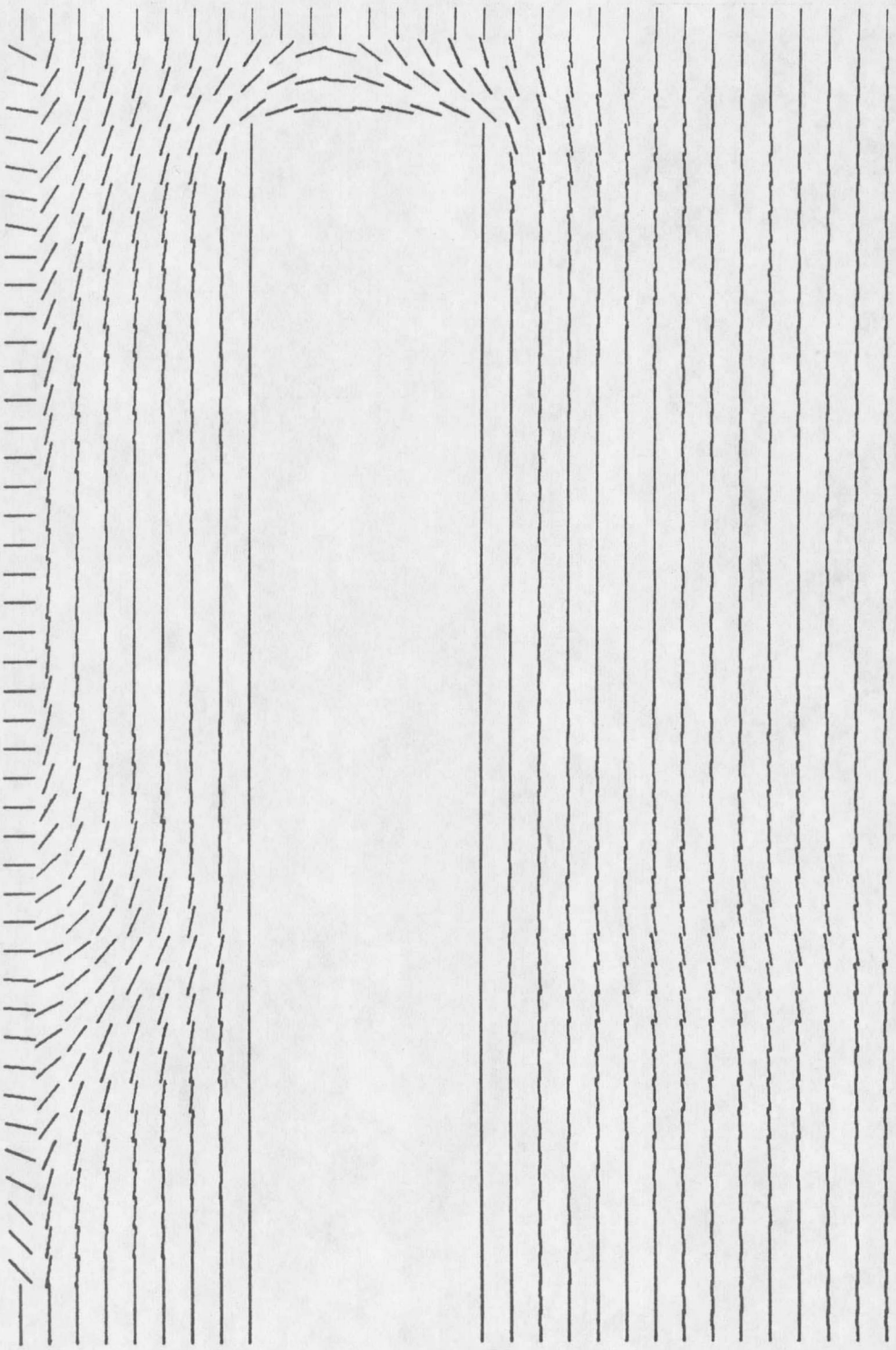

Figure 20. Flow Graph of Square Break (4 mm.)

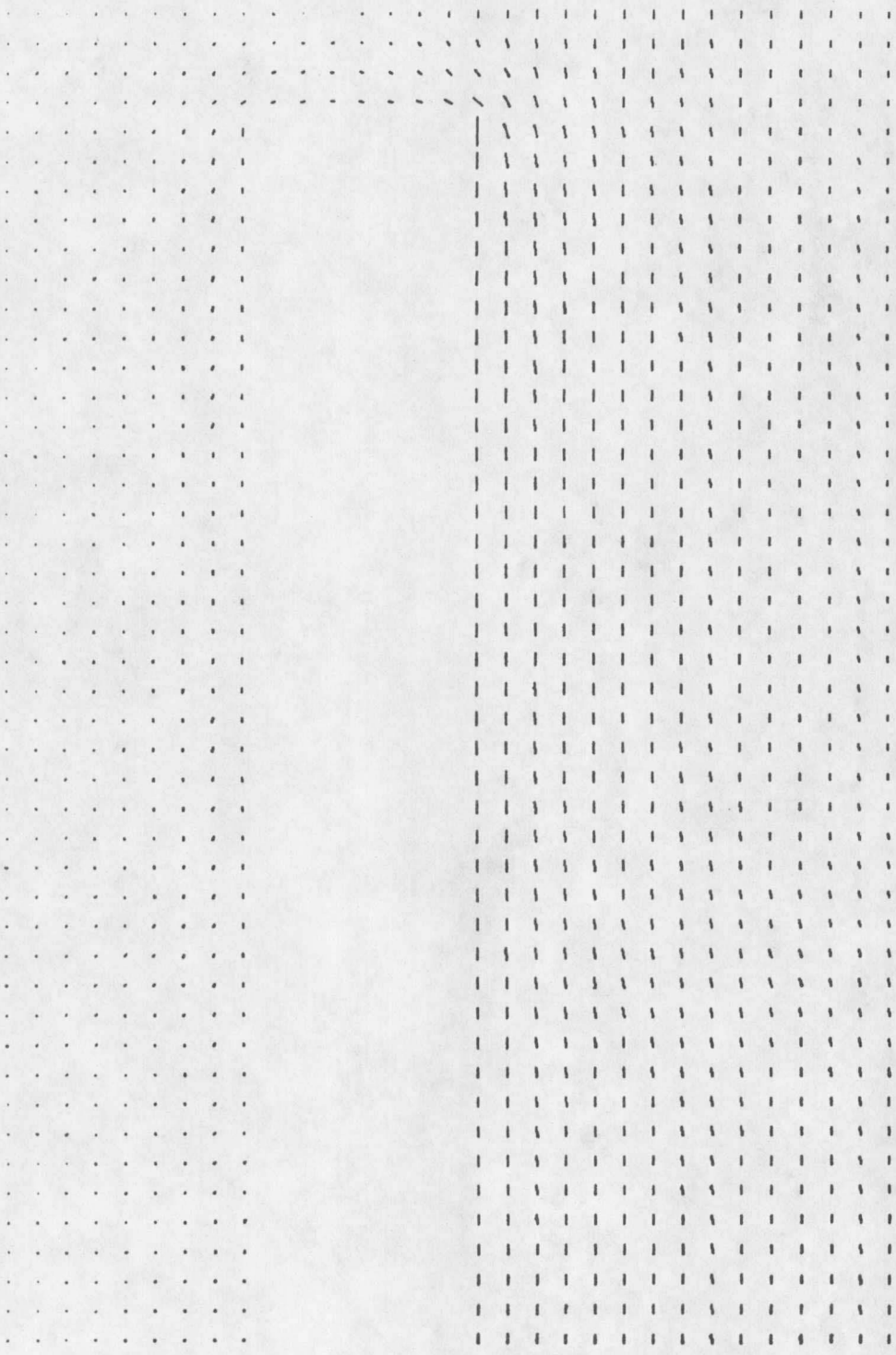

Figure 21. Magnitude and Flow Graph of Square Break (4 mm.)

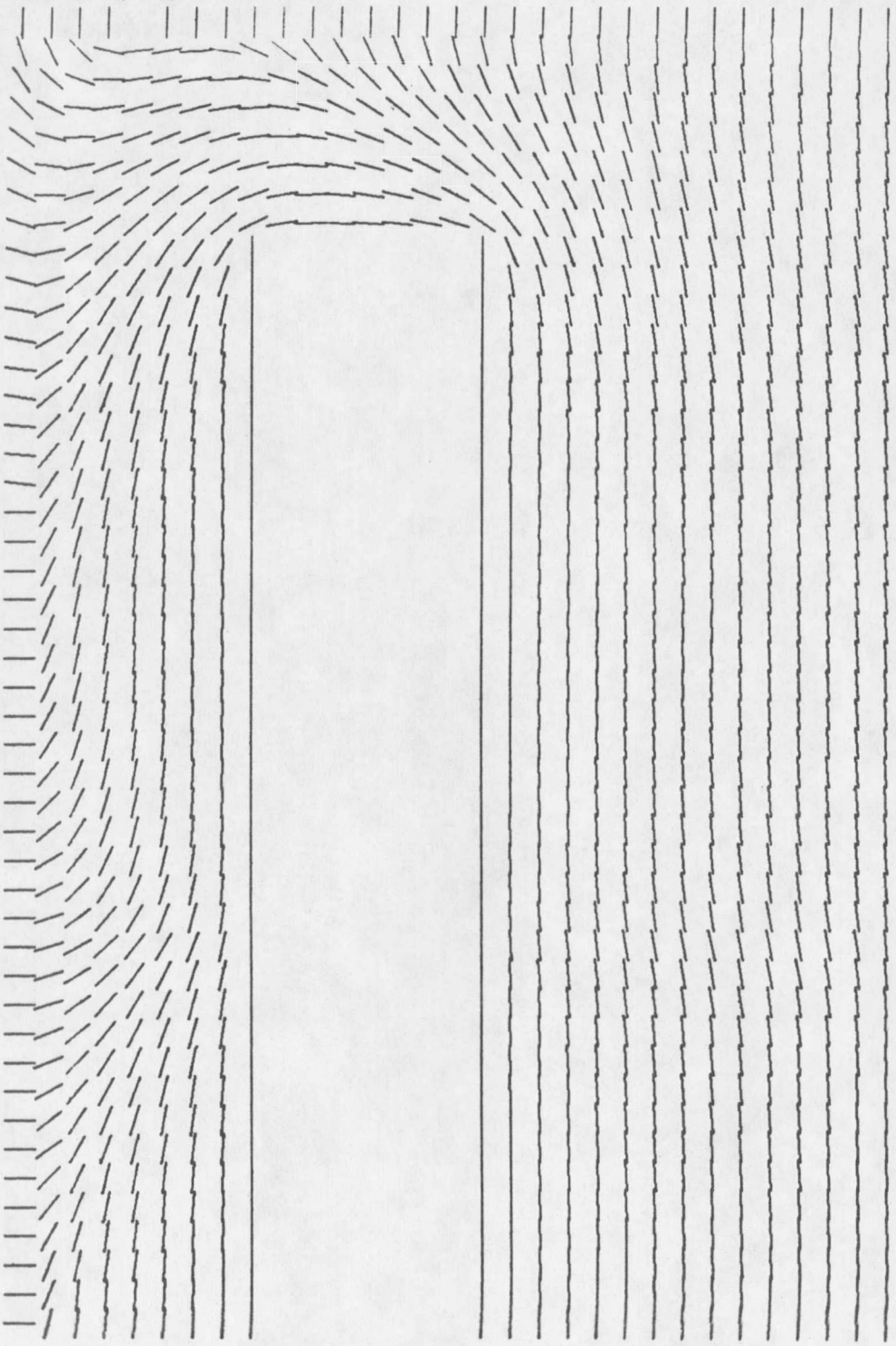

Figure 22. Flow Graph of Square Break (8 mm.)

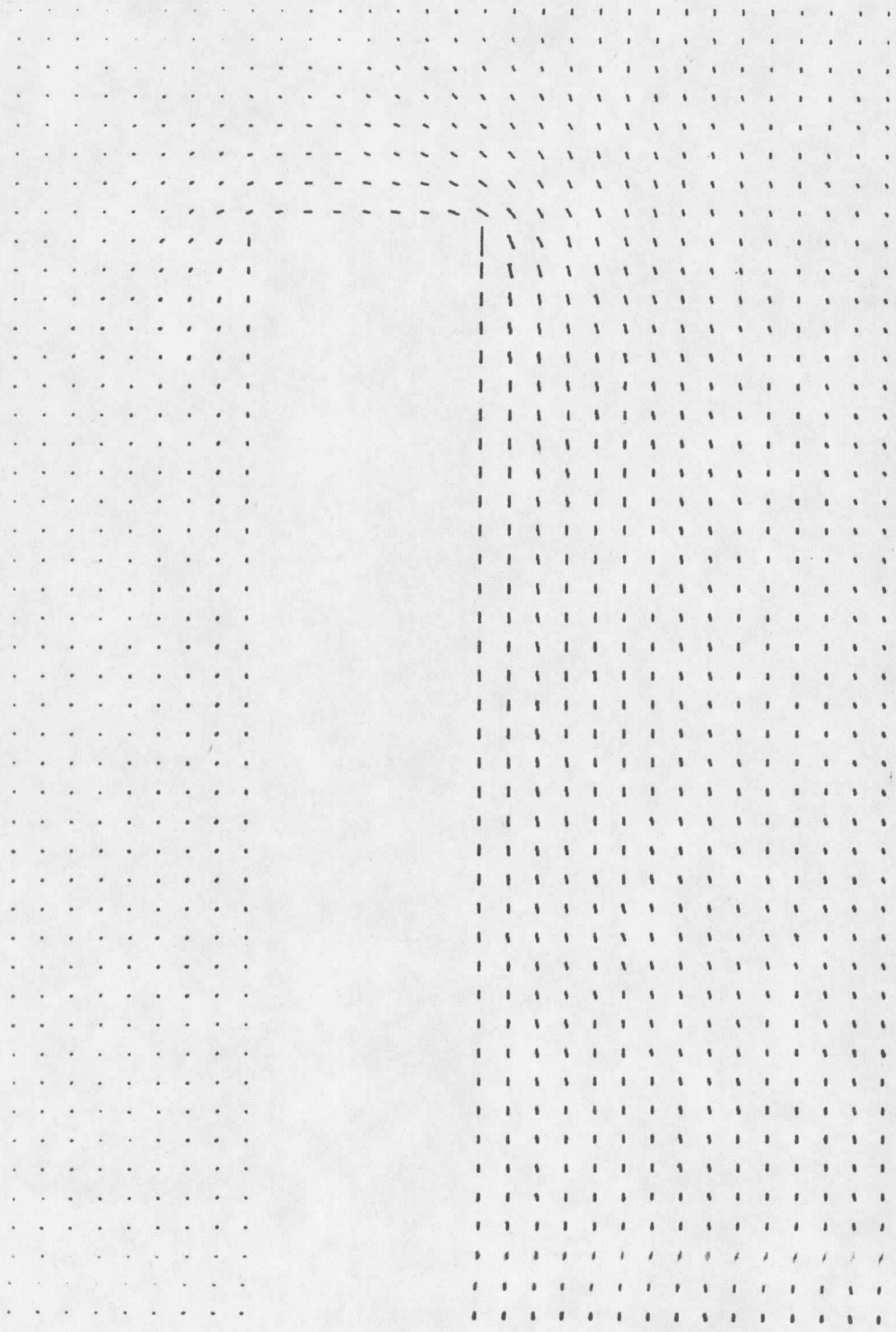

Figure 23. Magnitude and Flow Graph of Square Break (8 mm.)

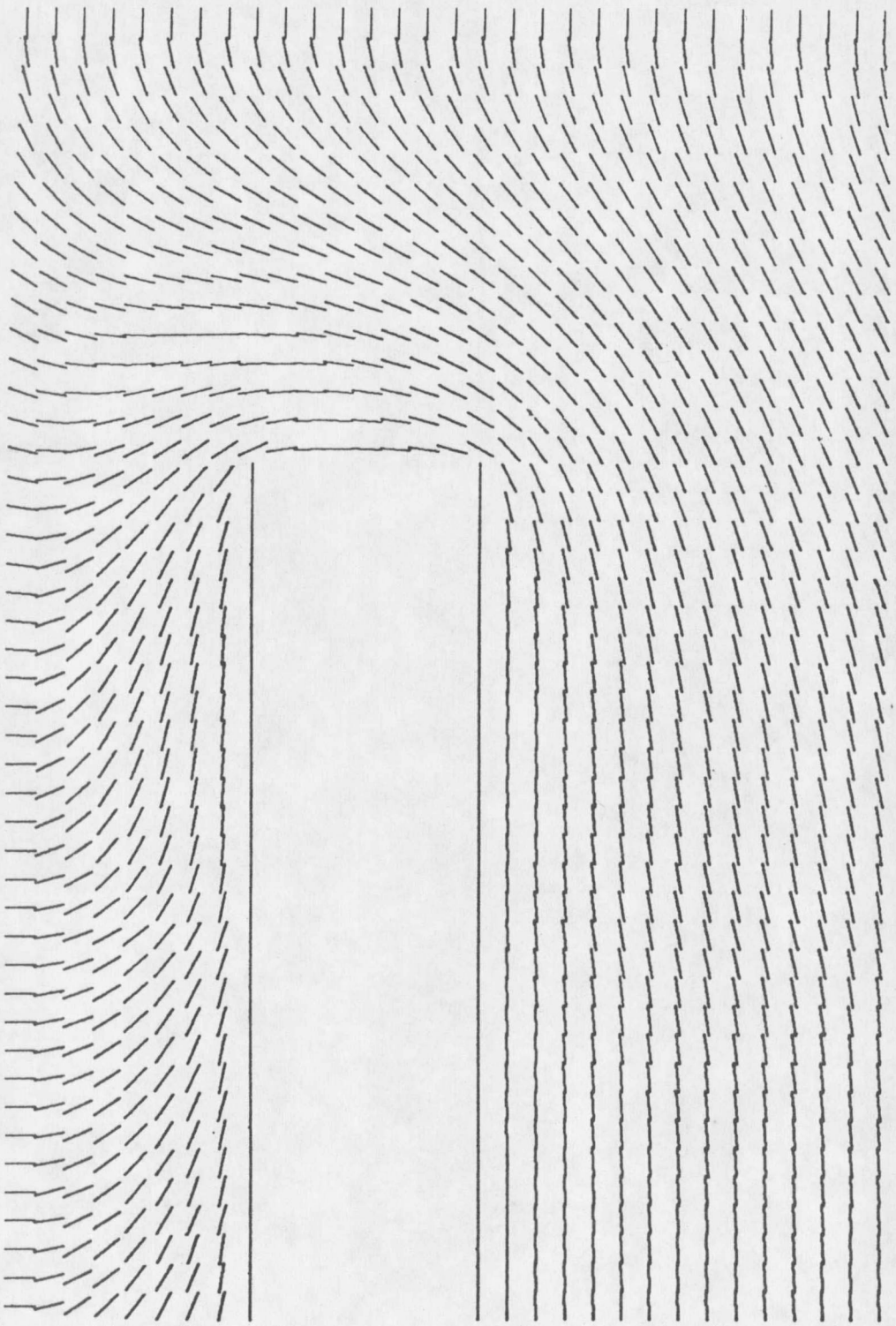

Figure 24. Flow Graph of Square Break (16 mm.)

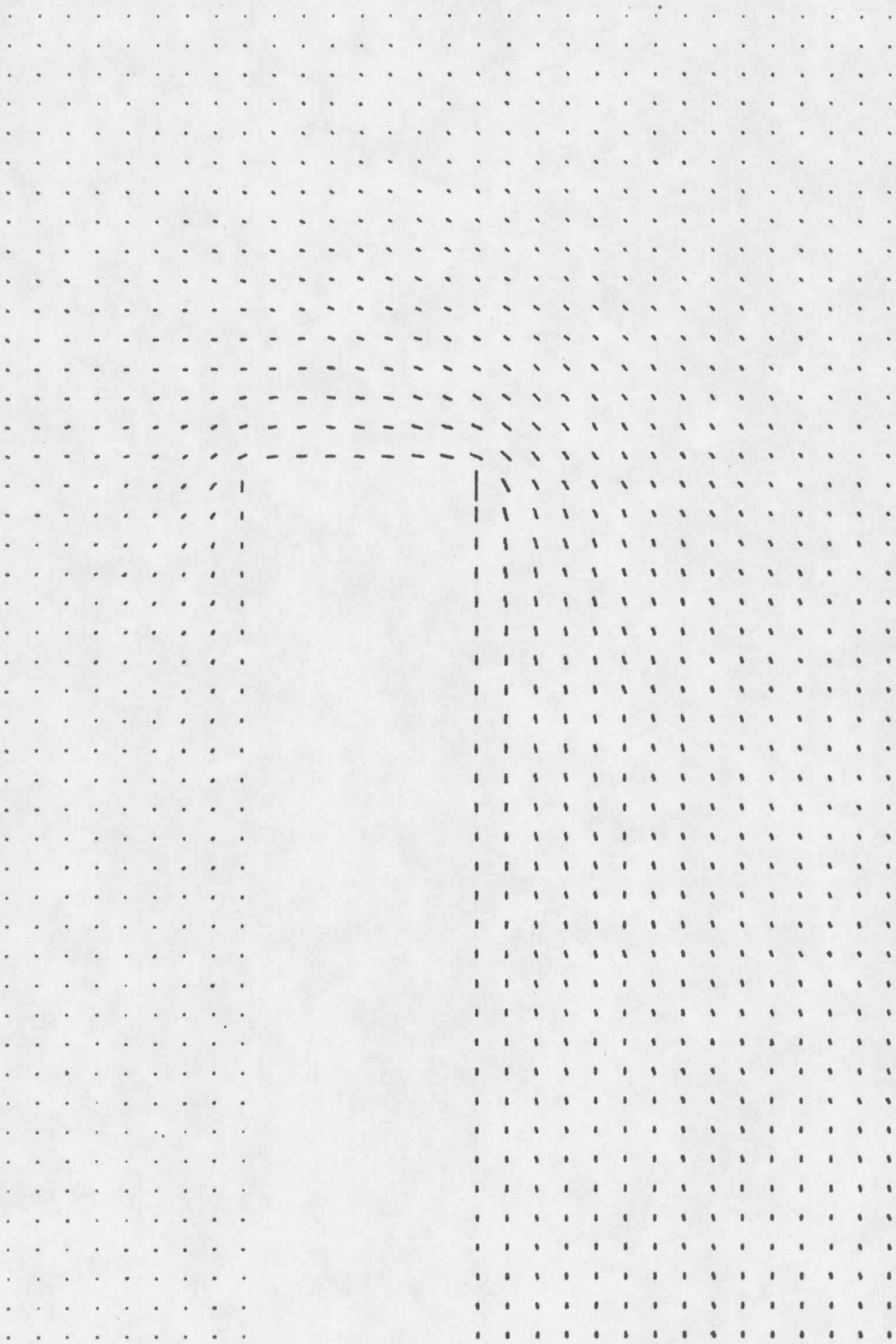

Figure 25. Magnitude and Flow Graph of Square Break (16 mm.)

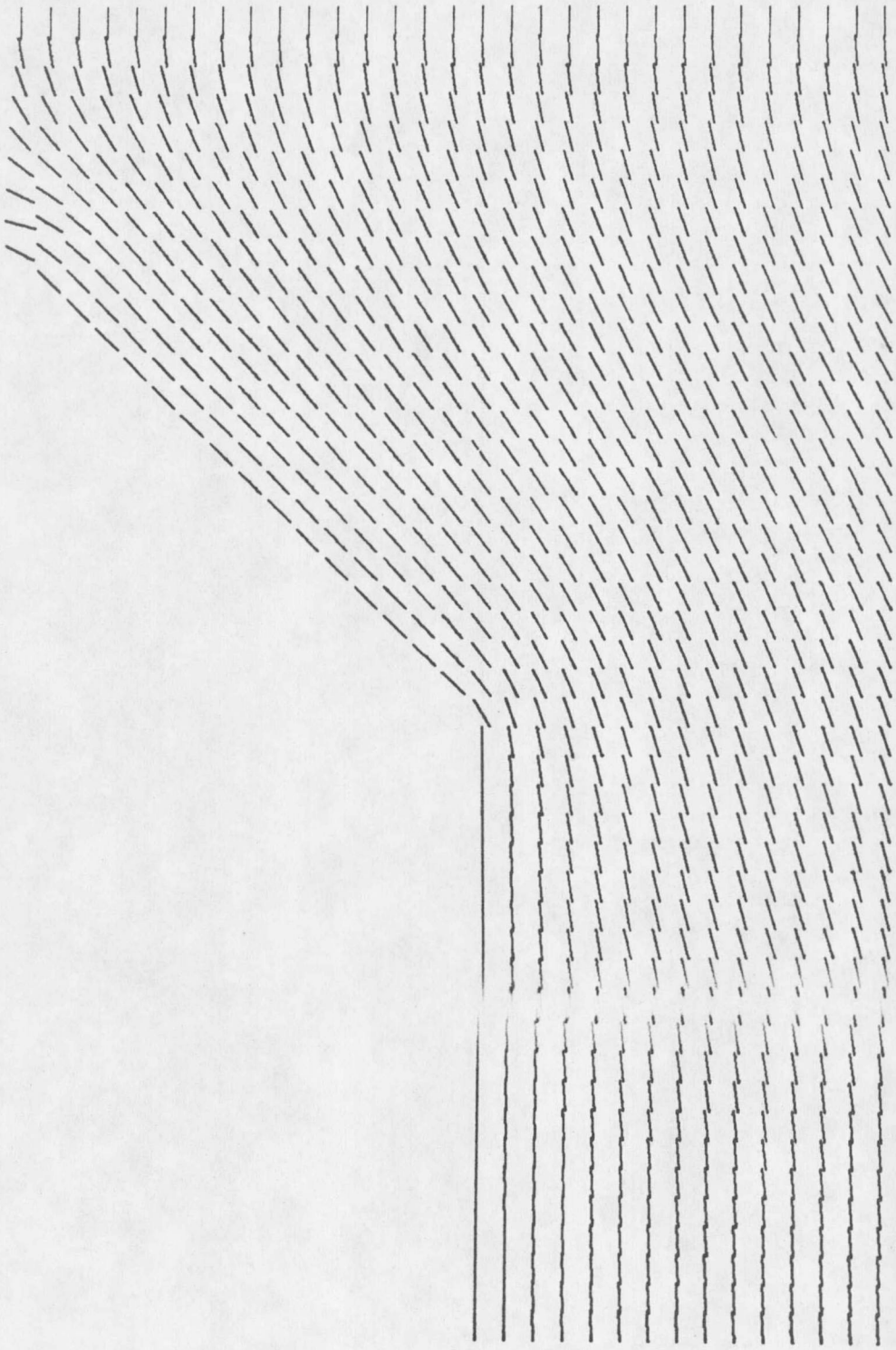

Figure 26. Flow Graph of Male-Male Break

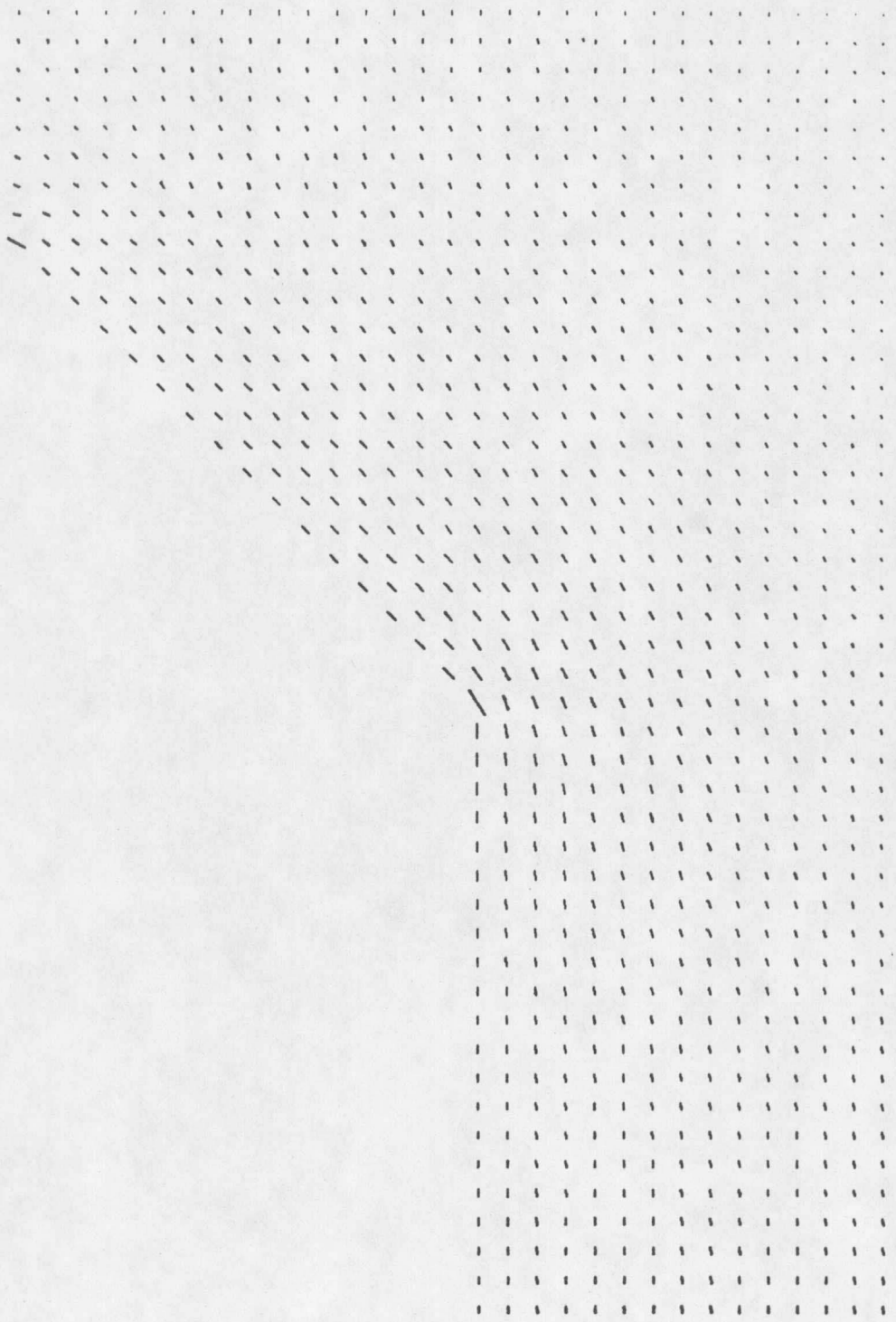

Figure 27. Magnitude and Flow Graph of Male-Male Break

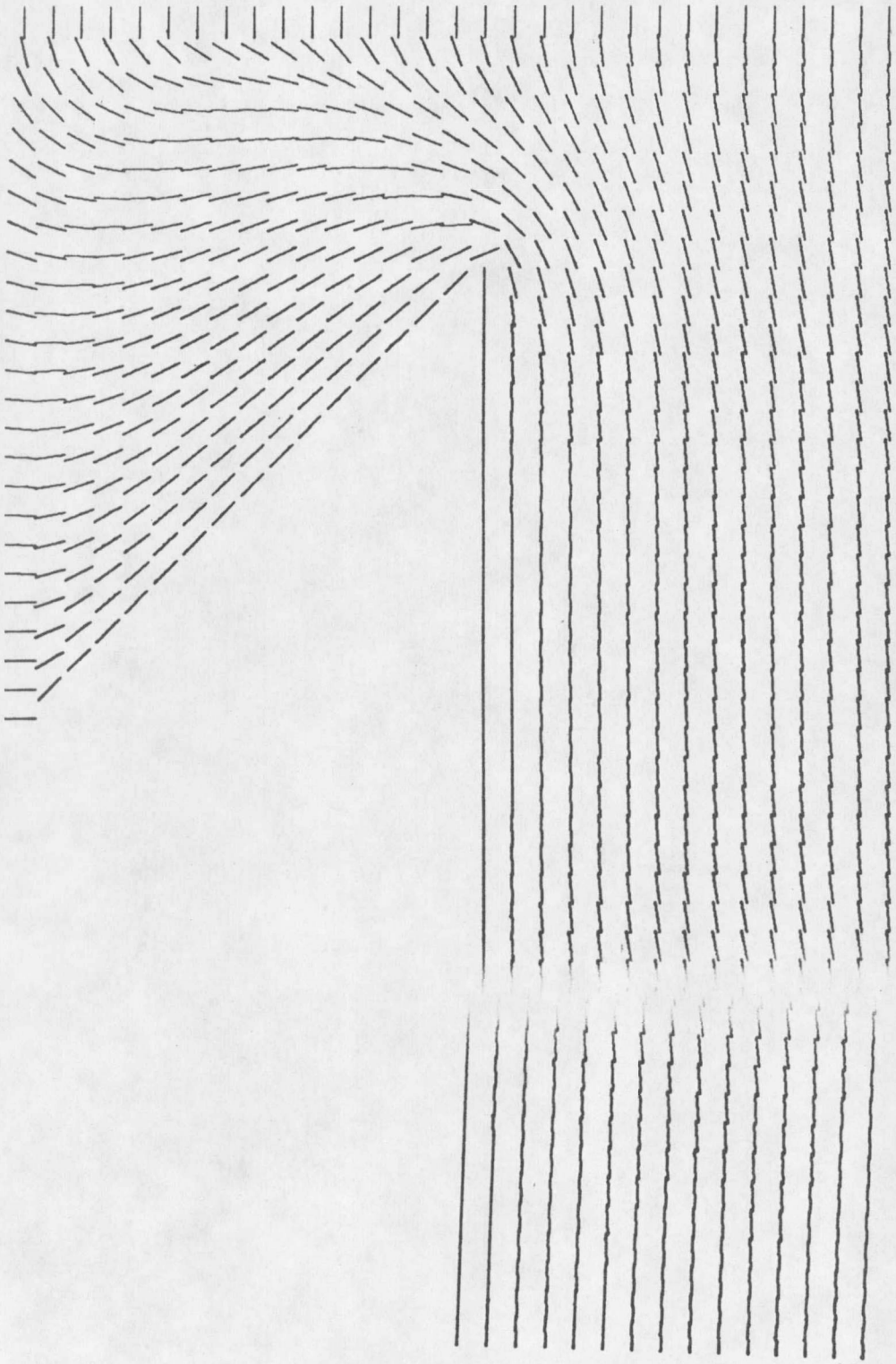

Figure 28. Flow Graph of Female-Female Break

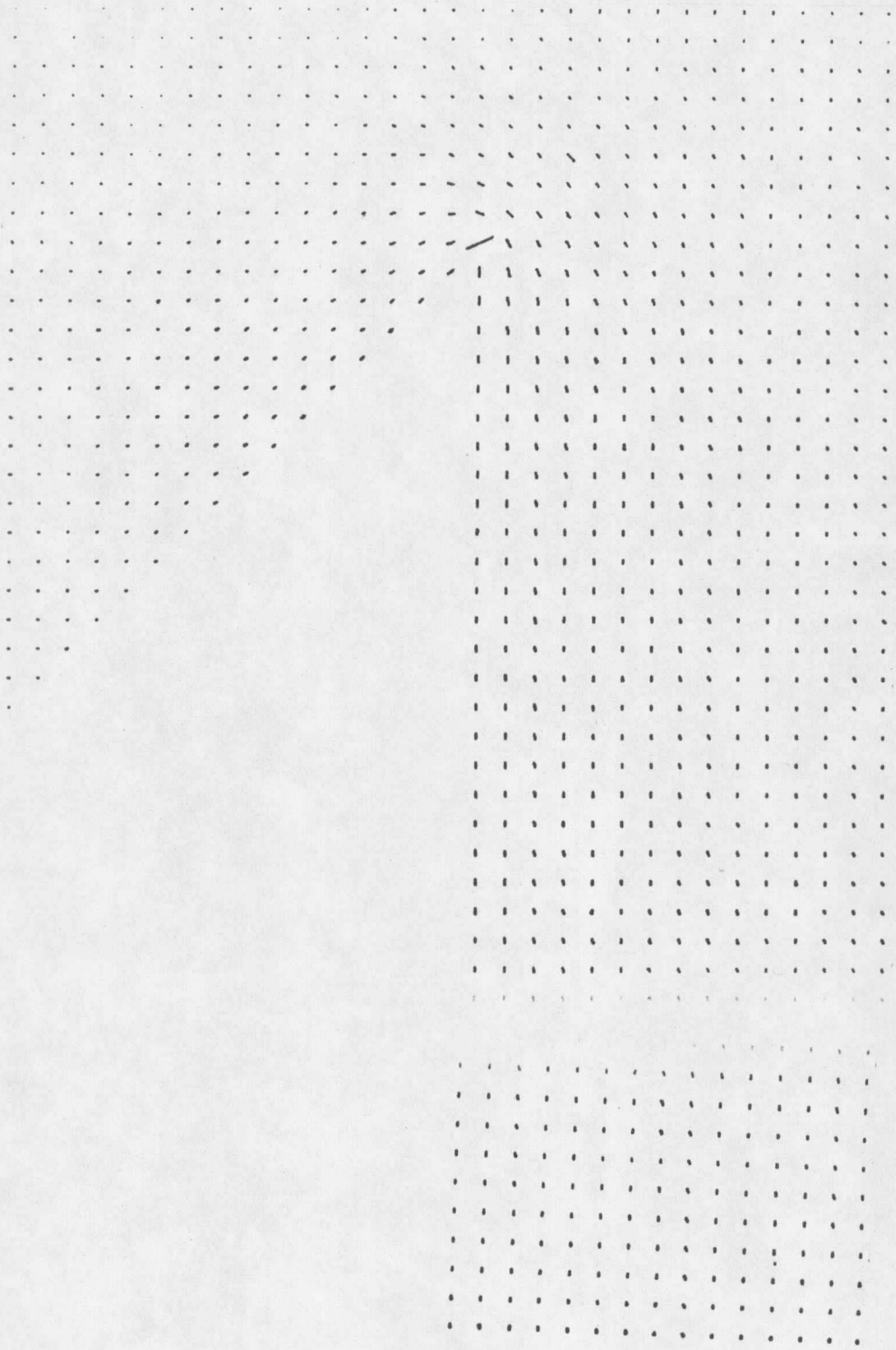

Figure 29. Magnitude and Flow Graph of Female-Female Break

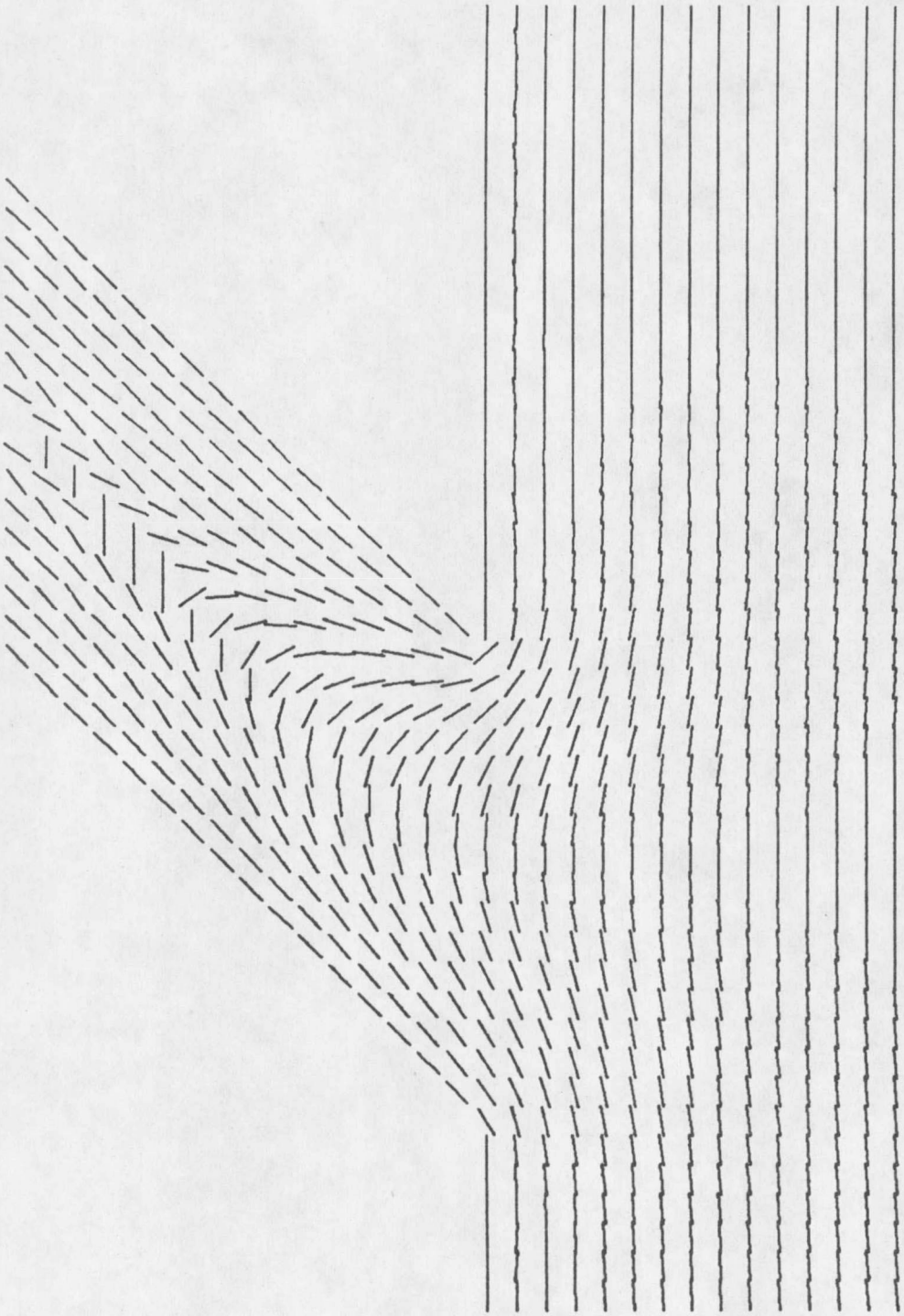

Figure 30. Flow Graph of Slanted Break

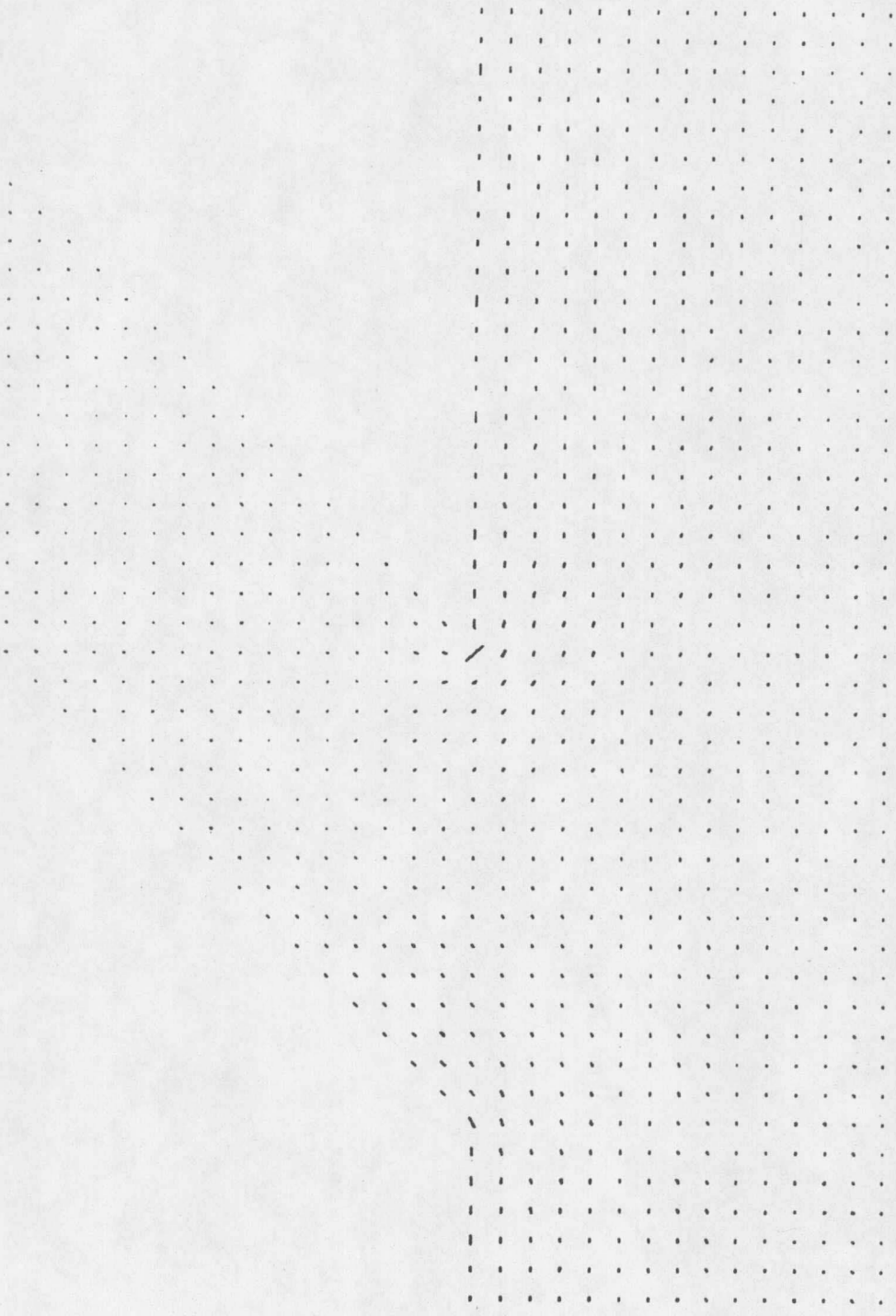

Figure 31. Magnitude and Flow Graph of Slanted Break

APPENDIX E

TWO DIMENSIONAL GRAPHS OF THE MAGNITUDE OF THE INDUCED CURRENT DENSITY FOR THE FEMALE-FEMALE BREAK WITH INTERMEDULLARY CANAL

APPENDIX E

TWO DIMENSIONAL GRAPHS OF THE MAGNITUDE OF THE INDUCED CURRENT DENSITY FOR THE FEMALE-FEMALE BREAK WITH INTERMEDULLARY CANAL

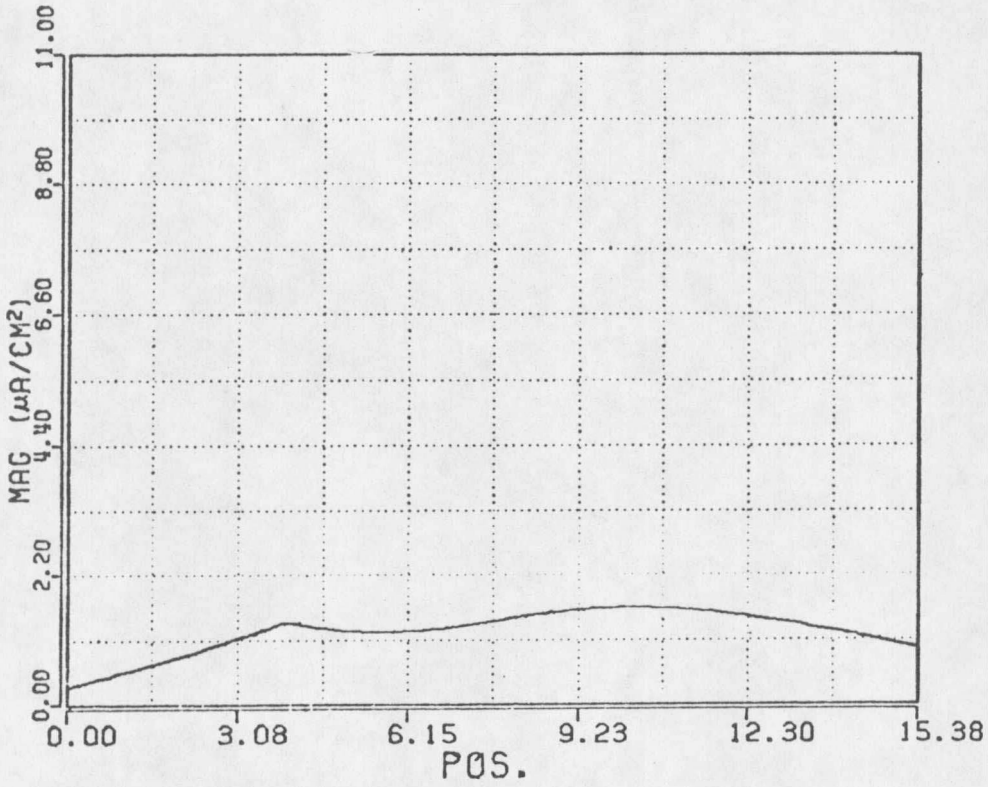

Figure 32. Graph along Centerline of Break

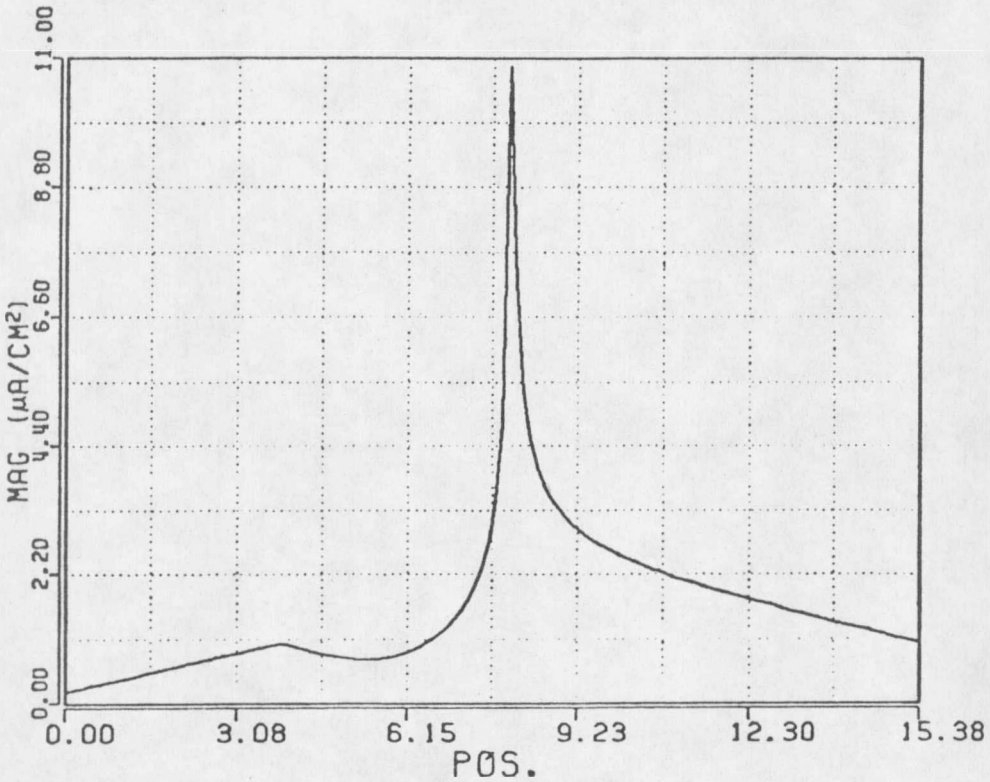

Figure 33. Graph of Slice Containing Outside Tip

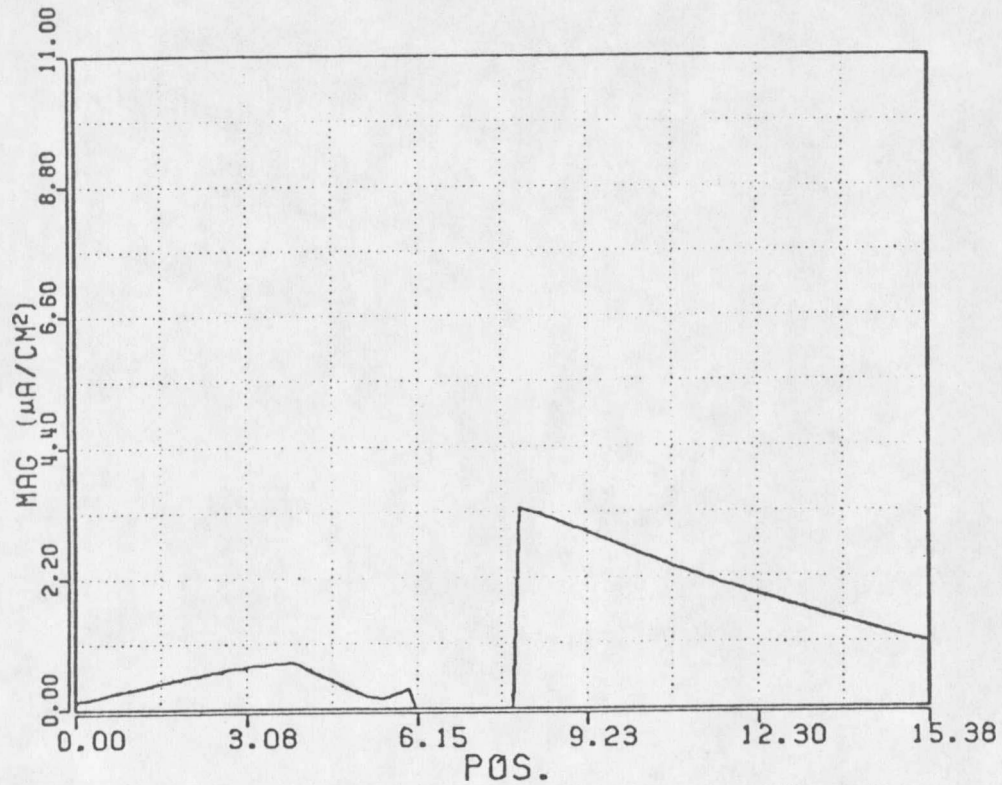

Figure 34. Graph of Slice Containing Center of Bone Face

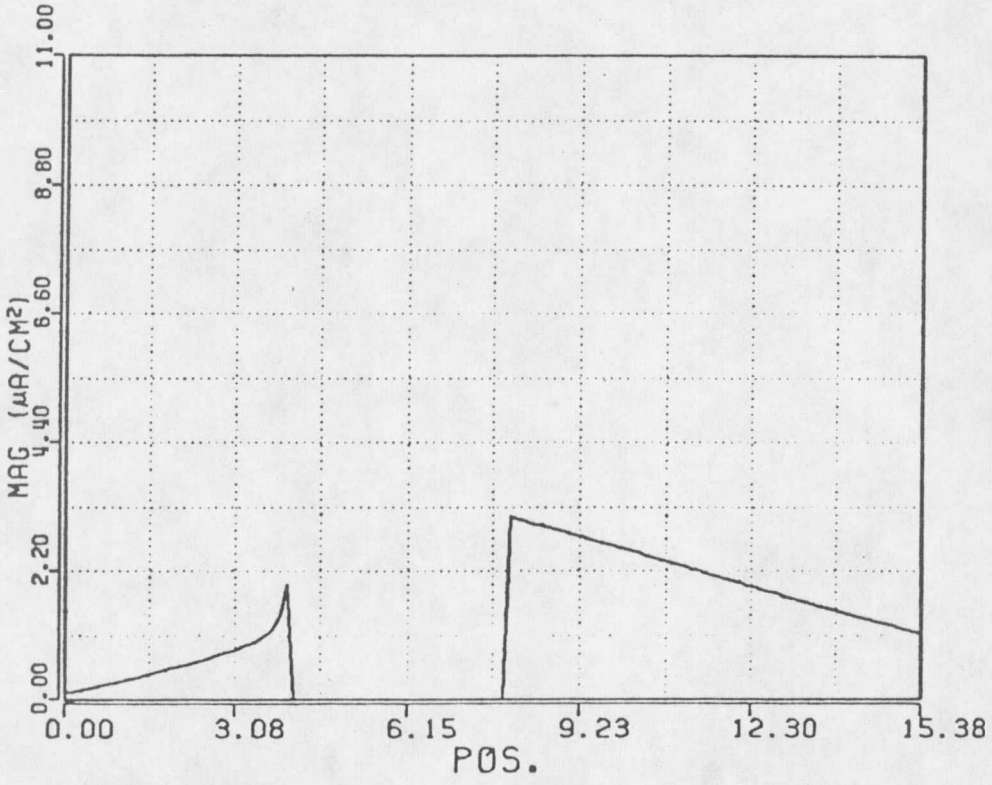

Figure 35. Graph of Slice Containing Inside Tip

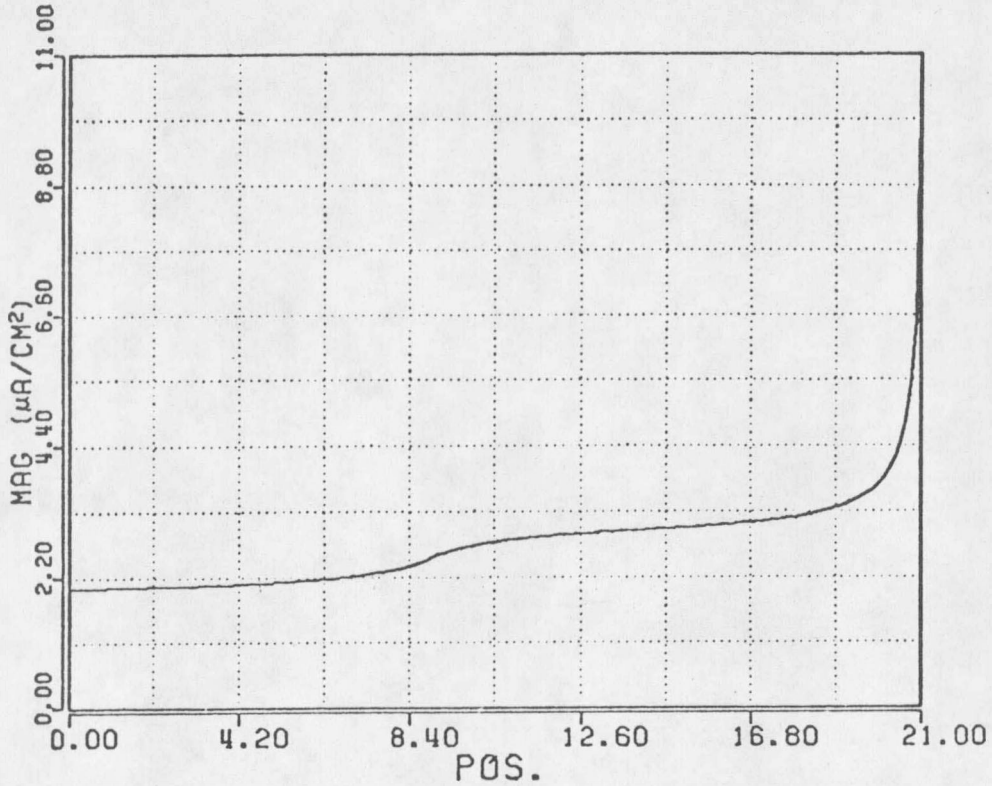

Figure 36. Graph of Outside Edge of Bone to Tip

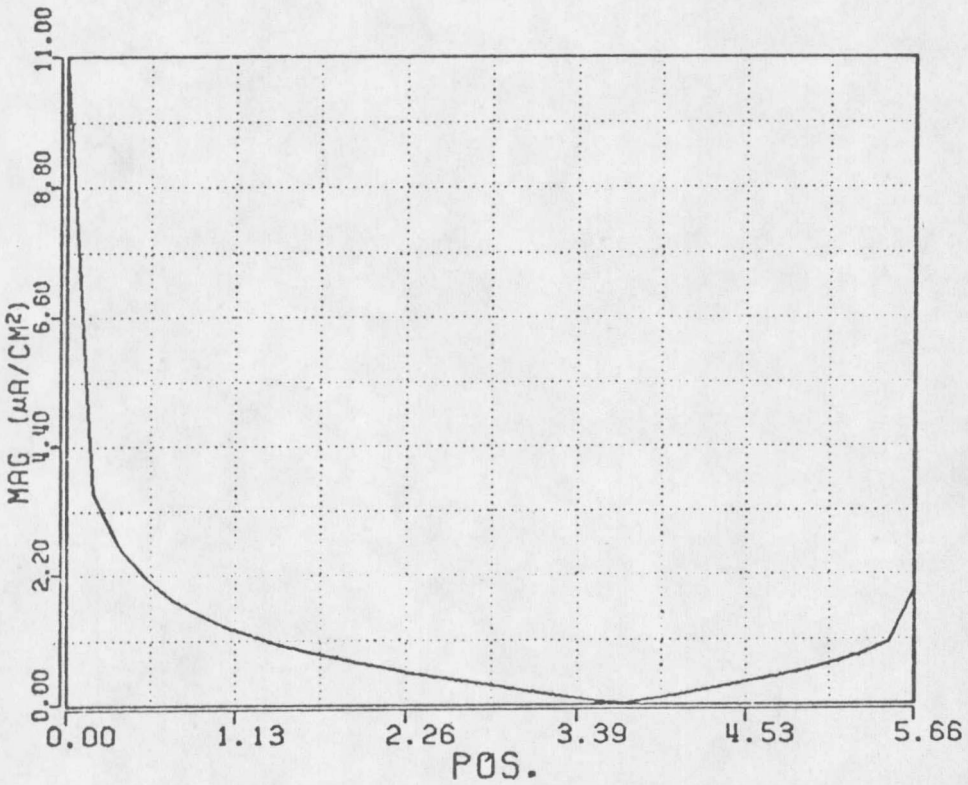

Figure 37. Graph of Bone Face from Outside to Inside

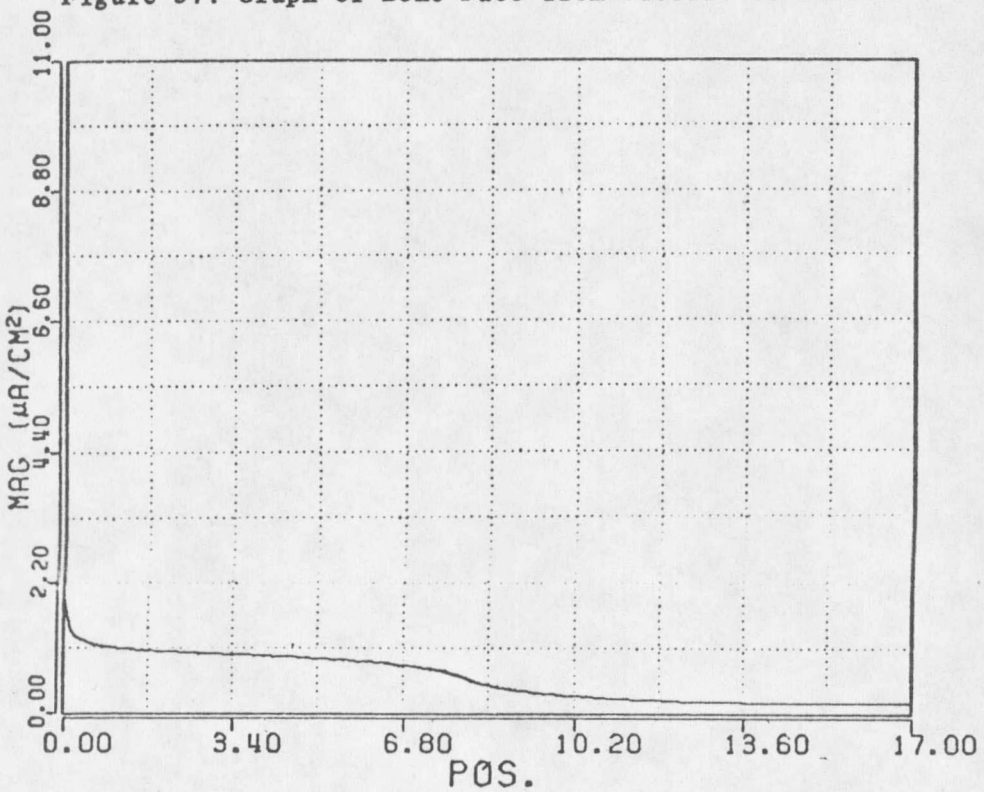

Figure 38. Graph along Edge of I.M. Canal

APPENDIX F

THREE DIMENSIONAL VIEWS OF THE MAGNITUDE OF THE INDUCED CURRENT DENSITY FOR THE FEMALE-FEMALE BREAK WITH INTERMEDULLARY CANAL

APPENDIX F

THREE DIMENSIONAL VIEWS OF THE FEMALE-FEMALE BREAK WITH INTERMEDULLARY CANAL

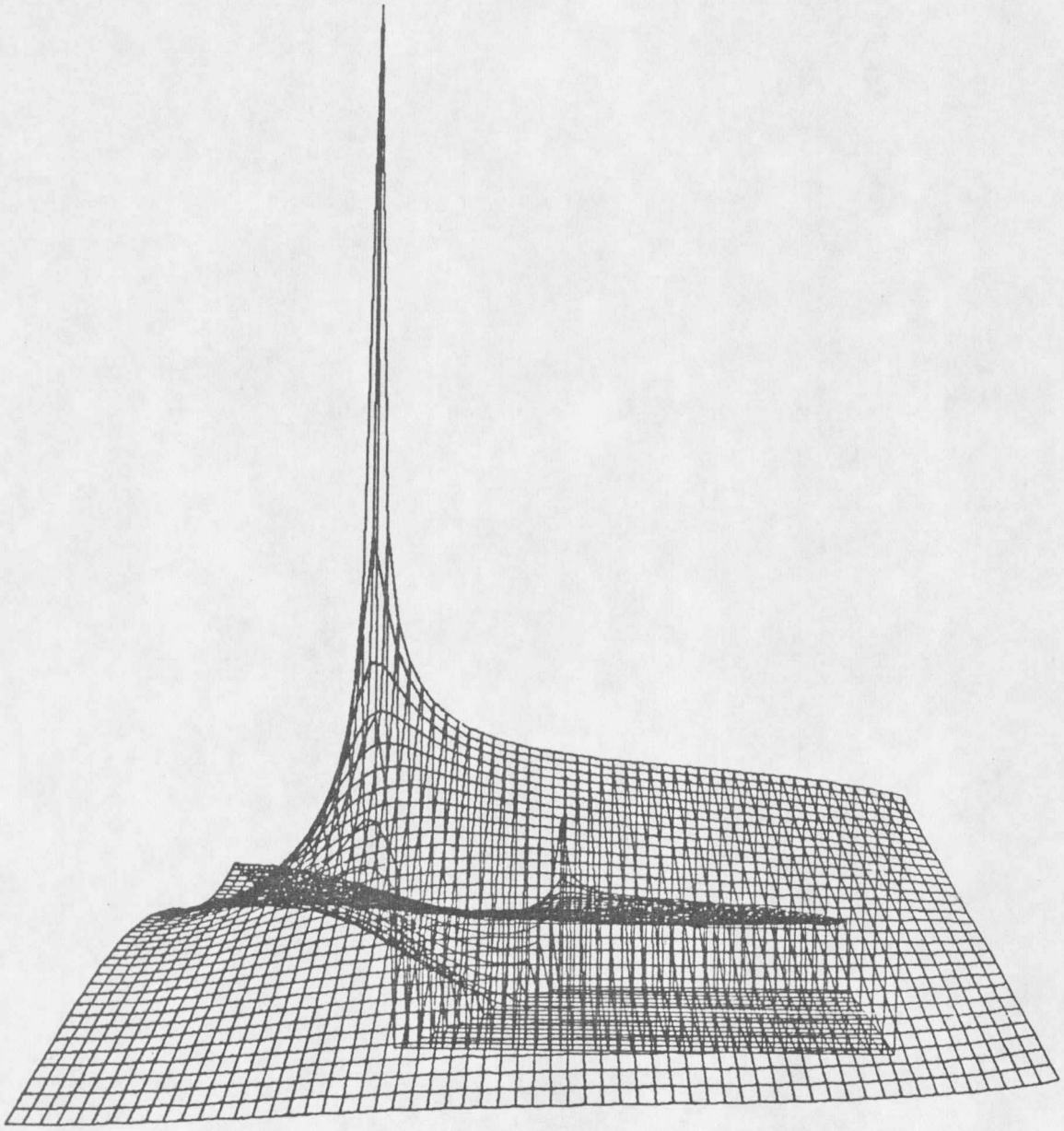

Figure 39. Three Dimensional View of Break Looking from Outside Toward the Outside Edge of Bone

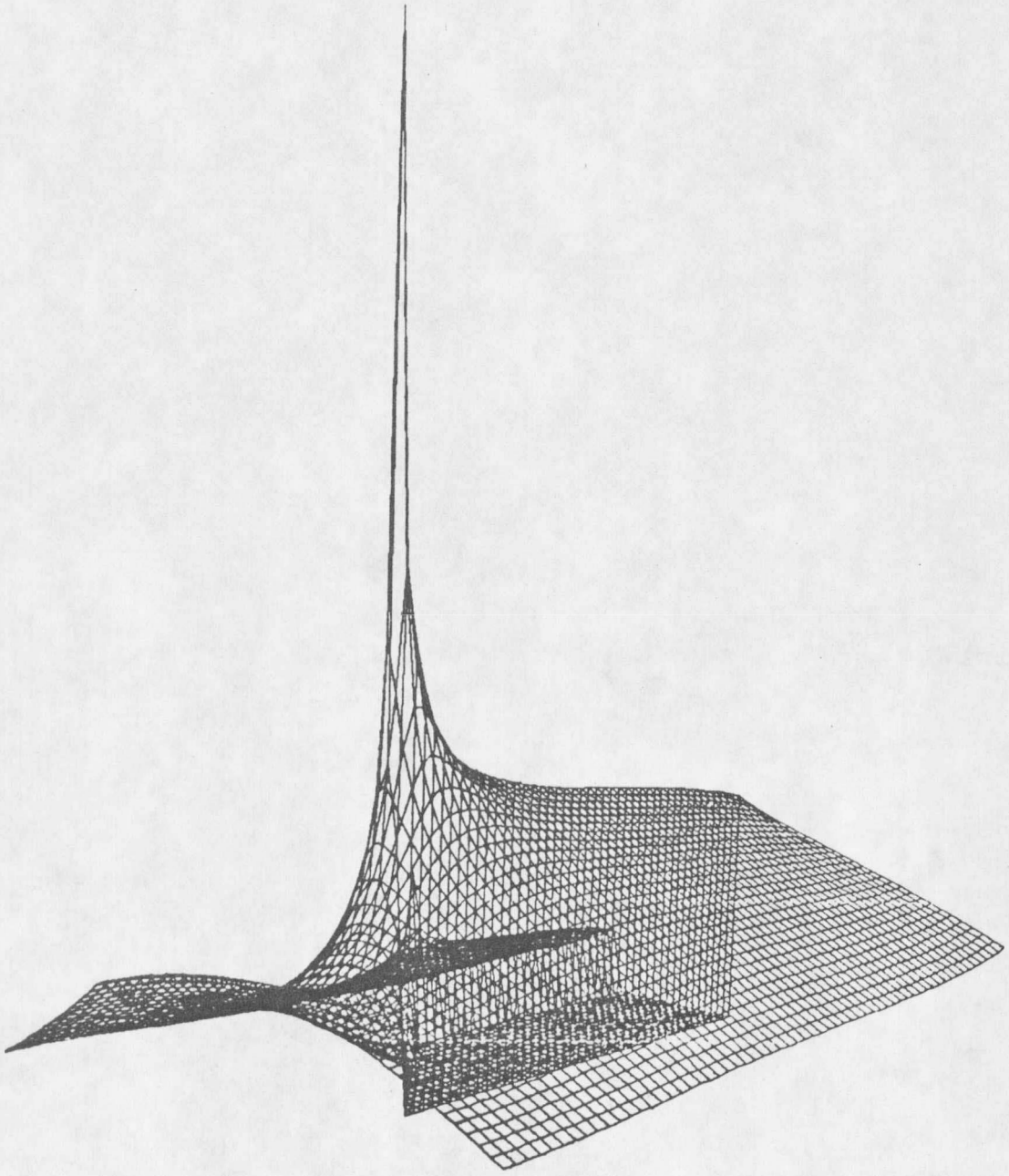

Figure 40. Three Dimensional View of Bone Looking from Outside Toward the Outside Corner of Bone

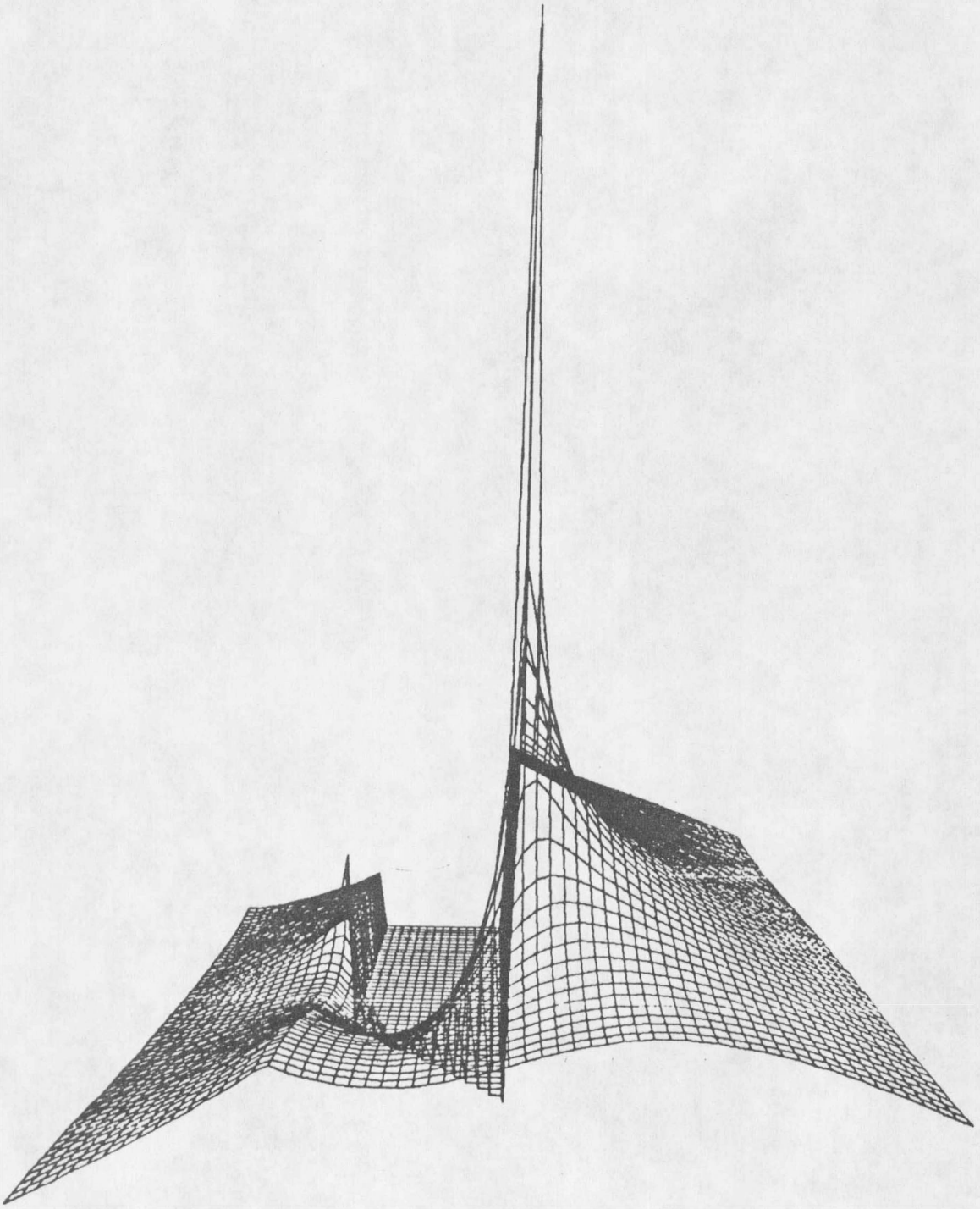

Figure 41. Three Dimensional View of Bone Looking from Center of Break Toward Bone Face

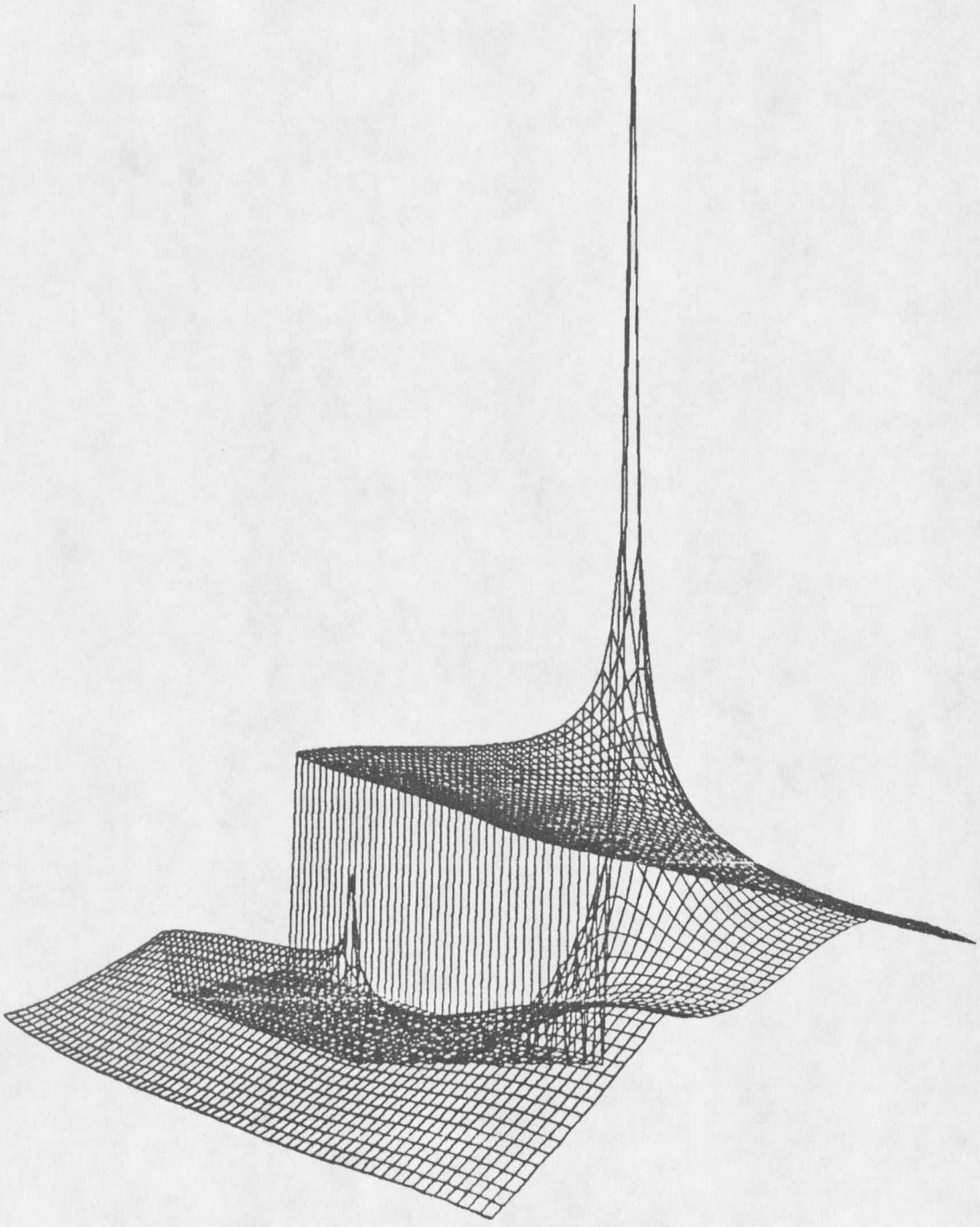

Figure 42. Three Dimensional View of Break Looking from Center of Break Toward Inside Corner

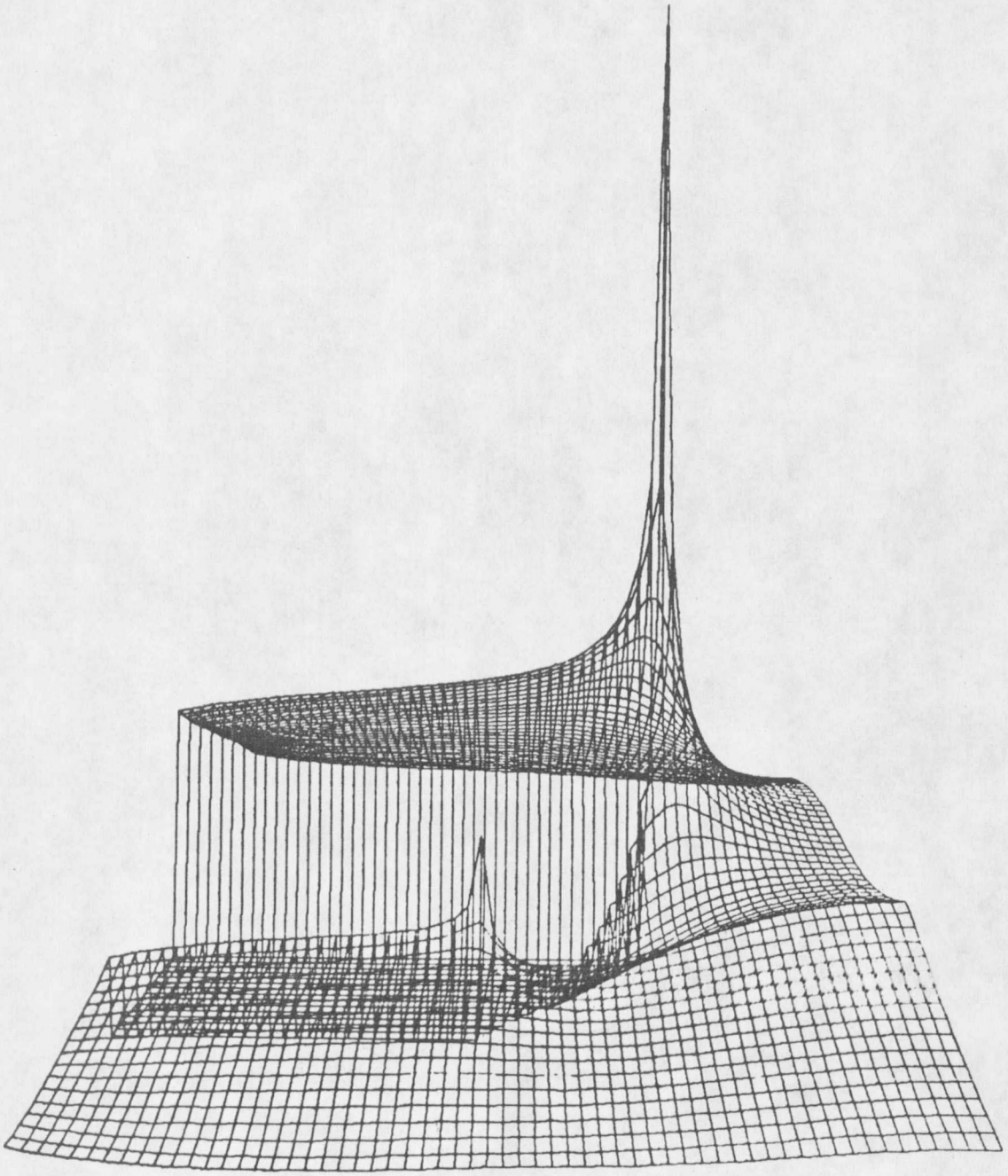

Figure 43. Three Dimensional View of Break Looking from Inside of I.M. Canal Toward Inside Edge

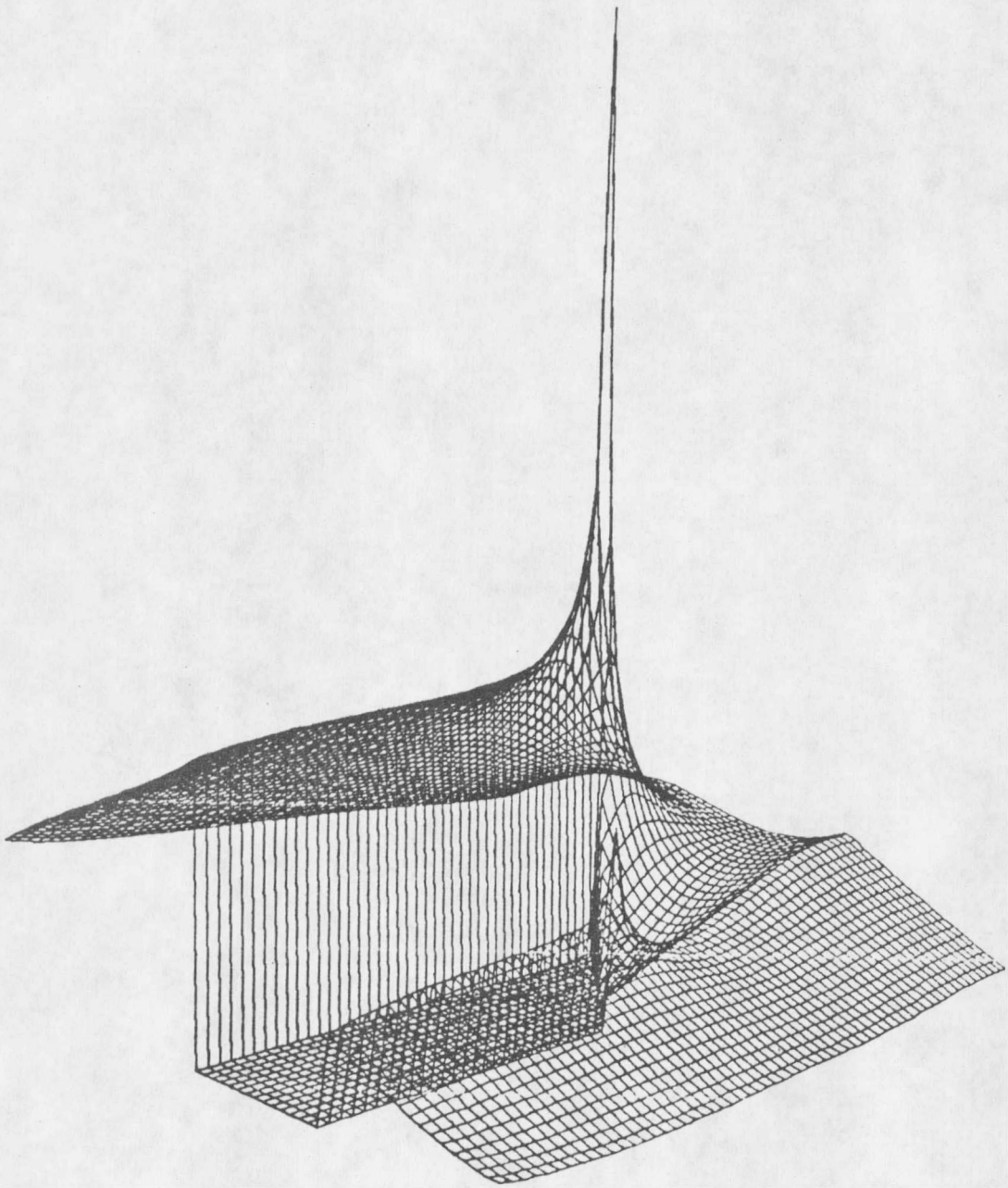

Figure 44. Three Dimensional View of Break Looking from Inside of I.M. Canal Toward Break

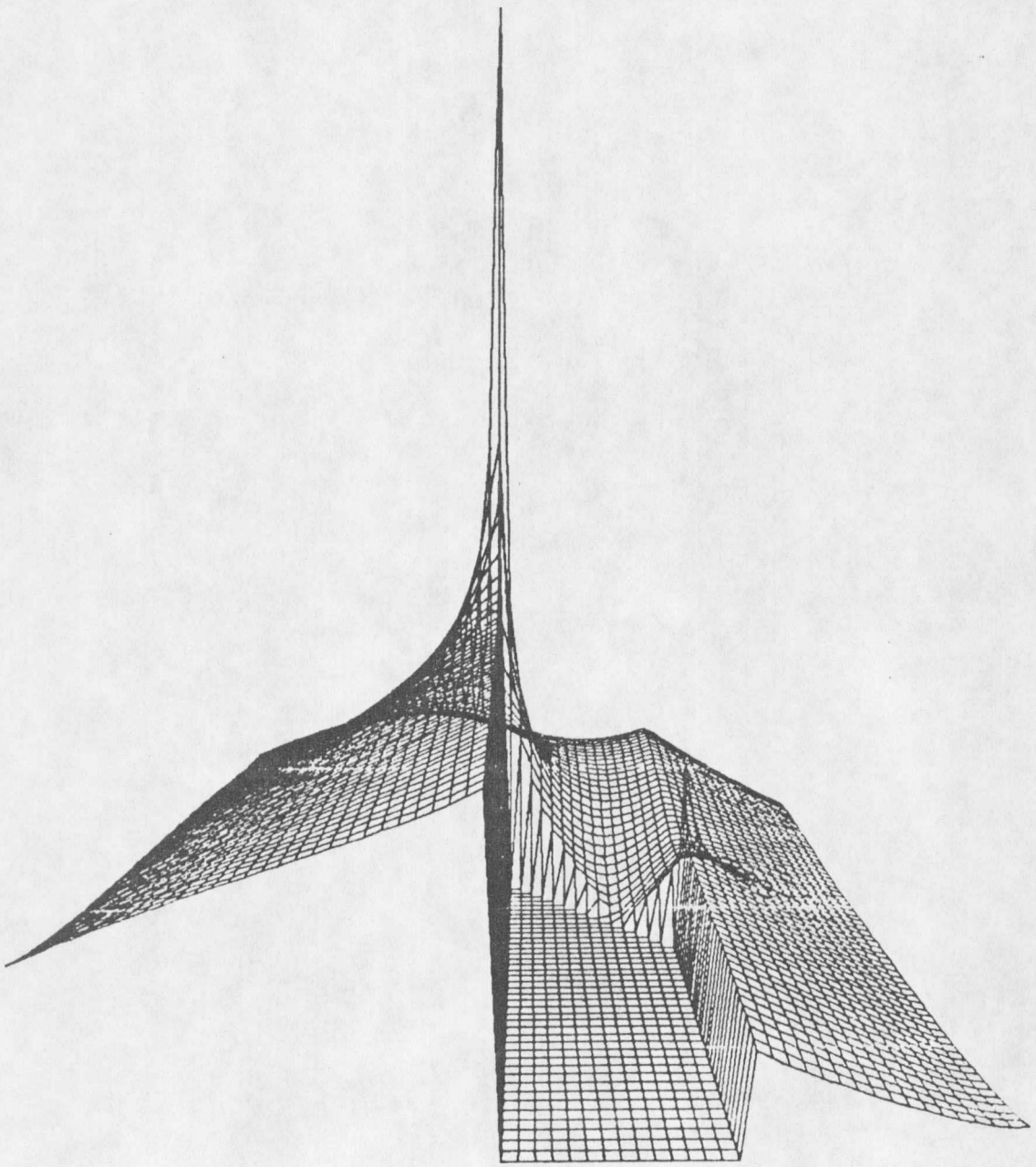

Figure 45. Three Dimensional View of Break Looking from Inside of Bone Toward Break

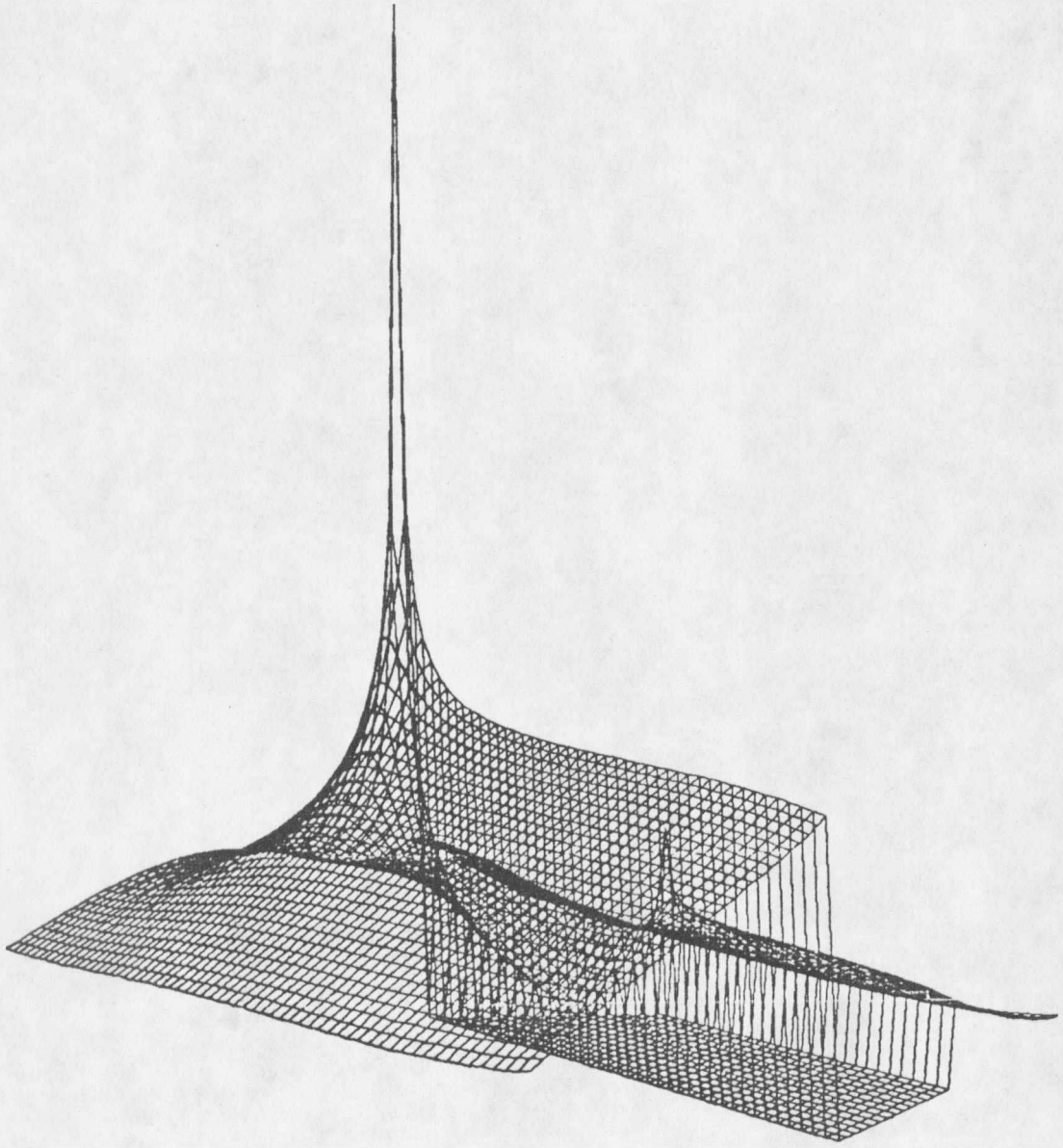

Figure 46. Three Dimensional View of Break Looking from Outside Toward Break

DATE	ISSUED TO